Method to characterize directional changes in arctic sea ice drift and associated deformation due to synoptic atmospheric variations using Lagrangian dispersion statistics

J.V. Lukovich[1], C.A. Geiger[2], D.G. Barber[1]

5 [1]Centre for Earth Observation Science, University of Manitoba, Winnipeg, R3T 2N2, CANADA
[2]College of Earth, Ocean, and Environment: Geography, University of Delaware, Delaware, 19716, USA

Correspondence to: J.V. Lukovich (Jennifer.Lukovich@umanitoba.ca)

Abstract. A framework is developed to assess the directional changes in sea ice drift paths and

10 associated deformation processes in response to atmospheric forcing. The framework is based on Lagrangian statistical analyses leveraging particle dispersion theory which tells us whether ice drift is in a subdiffusive, diffusive, or superdiffusive dynamical regime using single-particle (absolute) dispersion statistics. In terms of sea ice deformation, the framework uses two- and three-particle dispersion to characterize along and across-shear transport and differential kinematic parameters. The approach is

15 tested with GPS beacons deployed in triplets on sea ice in the southern Beaufort Sea at varying distances from the coastline in fall of 2009 with eight individual events characterized. One transition in particular follows the SLP high on 8 October in 2009 while the sea ice drift was in a superdiffusive dynamic regime. In this case, the dispersion scaling exponent (which is a slope between single-particle absolute dispersion of sea ice drift and elapsed time) changed from $\alpha \sim 3$ to $\alpha \sim 2$ as the SLP was

20 rounding its maximum pressure value. Following this shift in the scaling exponent there was a loss in synchronicity between sea ice drift and atmospheric motion patterns. The tools developed in this study provide a unique characterization of sea ice processes in the southern Beaufort Sea with implications for ice hazard assessments and forecasting applications required by marine transportation and indigenous use of near shore Arctic areas.

1 Introduction

Central to our understanding of changes in the arctic sea ice cover in response to a changing climate and continued anthropogenic forcing is an understanding of sea ice drift and deformation, namely sea ice dynamics. Accelerated ice drift speed over the past several decades reflects a weaker and more mobile

5 ice cover associated with the loss of multiyear ice and changes in atmospheric circulation (Hakkinen et al. 2008; Barber et al., 2009; Rampal et al. 2009b; Spreen et al., 2011; Kwok et al., 2013). Sea ice deformation, or spatial gradients in the ice drift field, associated with opening and closing in the ice cover due to sea ice divergence and convergence, influences moisture and heat exchange between the ocean and atmosphere, ice ridging, sea ice thickness and redistribution (Hutchings et al., 2011, Bouillon

10 et al., 2015) with implications ice hazard detection, and pollutant and contaminant transport. In the Beaufort Sea region, sea ice dynamics is governed by large-scale anticyclonic circulation of the Beaufort Gyre, with reversal to cyclonic circulation throughout the annual cycle (LeDrew et al. 1991; Preller and Posey, 1989; Proshutinsky et al., 2015).

When the ice cover on polar seas changes abruptly, navigation channels are altered as a result of

15 ice-ice and ice-coastline momentum and energy flux exchanges (e.g., The Polar Group, 1980; Hwang, 2005; McPhee, 2012), air-sea heat exchanges increase (e.g., Carmack et al., 2015), and newly opened leads vent high moisture into the atmosphere as a strong mass exchange process (Bourassa et al., 2013). Understanding how these changes develop and relate to the orientation of a coastline is essential when diagnosing response patterns. For clarity, directional change in this study refers to changes in the ice

20 drift path relative to storm tracks, which have typical duration on the order of days and recurrence rates on the order of several days to weeks.

Arctic air-ice-sea interactions on synoptic timescales (several days to weeks) are governed by a force balance consisting of three interactive components: i) sea ice motion, ii) a confining coastline, and iii) atmospheric forcing. Previous studies have examined sea ice drift and deformation response to

25 atmospheric forcing and coastline geometry on varying timescales (Overland et al., 1995; Richter-Menge et al., 2002; Geiger and Perovich, 2008; Hutchings et al., 2011). In an assessment of springtime sea ice drift in a region to the west of the Antarctic Peninsula, Geiger and Perovich (2008) identified low-frequency motion in response to atmospheric forcing and coastal geometry associated with

regional-scale transport, and higher-frequency near-inertial oscillatory motion associated with mixing. On regional and synoptic scales, Richter-Menge et al. (2002) also distinguish between translational and differential motion associated with shear zones and discontinuities in the ice drift characteristics in the southern Beaufort Sea.

5   The role of forcing (wind stress) and coastline geometry in establishing coherence in lead patterns/fractures in the ice cover captured by sea ice deformation has also been explored in past studies (Overland et al., 1995; Hutchings et al., 2005, 2011). Overland et al. (1995) demonstrated that in the Beaufort Sea for spatial scales: i) exceeding 100 km the sea ice cover moves as an aggregate; ii) less than 100 km the ice cover moves as an aggregate or discrete entity based on whether an elliptic

10   (homogeneous) or hyperbolic (discrete) regime is established relative to the coastline (ice-coast interactions); and iii) on the order of 1 km the ice cover is characterized by floe (ice-ice) interactions. Through analysis of a nested beacon configuration and array with spatial scales ranging from 10 km to 140 km as part of the late winter (April) 2007 Sea Ice Experiment: Dynamic Nature of the Arctic (SEDNA) campaign in the Beaufort Sea, Hutchings et al. (2011) demonstrated coherence between 140

15   km and 20km divergence arrays for time periods of up to 16 days in March. Over shorter (sub-synoptic) timescales from May 2007 onward, nested buoy arrays captured the loss of connectivity in the sea ice cover associated with the winter-to-summer transition during a substantial ice-loss year (Stroeve et al., 2008). From these earlier findings, we see a need for an approach to describe structure in a flow (in this case ice drift) field to quantify changes in the ice cover in the context of sea ice drift and deformation,

20   based on Lagrangian dispersion statistics, and one-, two-, and three-particle dispersions statistics in particular, which we focus on specifically below.

1.1 Lagrangian dispersion statistics

Central to developing the tools required to understand sea ice drift and deformation in response to atmospheric forcing and ice-coastline interactions are diagnostics and in the case of drifting buoys, a

25   Lagrangian framework to quantify spatiotemporal changes in the ice cover. Traditionally used to characterize patterns and structure in atmospheric and oceanic dynamical phenomena, Lagrangian dispersion statistics identify topological and thus quantify dynamical features in a flow field (LaCasce,

2008 and references therein). Previous studies have also used Lagrangian dispersion and ice beacon trajectories to quantify sea ice drift and deformation in the Arctic (Colony and Thorndike, 1984, 1985; Rampal, 2008, 2009a,b, 2016; Lukovich et al., 2011, 2014, 2015). Single-particle (absolute) dispersion provides a signature of large-scale circulation and captures linear time-dependence in fluctuating velocity variance characteristic of turbulent diffusion theory (Taylor, 1921; Rampal et al., 2009); i.e., departures in ice fluctuating velocity statistics from turbulent diffusion are attributed to intermittency associated with sea ice deformation and internal ice stress (Rampal et al., 2009).

A two-particle (relative) dispersion analysis monitors sea ice deformation. Through evaluation of buoy pair separations as a proxy of strain-rate (divergence, convergence, and strain) components combined, two-particle dispersion demonstrates heterogeneity and intermittency in the sea ice deformation field associated with space/time coupling inherent in fracturing of the sea ice cover as described by sea ice mechanics (Rampal et al., 2008; Weiss, 2013; Weiss and Dansereau, 2017). Rampal et al. (2008) noted that a triplet or multiple-particle analysis is in addition necessary to illustrate the deformation and related small-scale kinematic features that develop in sea ice.

Three -particle dispersion and triplet areas in particular, such as are explored in this study, enable a distinction between the individual strain-rate tensor components of divergence, convergence, and shear. Specifically, sea ice divergence depicts open water formation and accompanying processes such as new ice growth, brine rejection to the ocean, and heat and moisture exchange; ice convergence depicts ridge and keel formation thus contributing to ice thickness (Stern and Lindsay, 2009; Kwok and Cunningham, 2012), with implications for ice hazard detection, oil spill and contaminant transport and shipping route assessments. Triplet areas also provide a signature of what is referred to by Thorndike (1986) as "nondivergent diffusive mixing" due to compressibility in the ice cover.

Early studies of oceanic circulation have used multiple particles to monitor small-scale deformation and mixing as opposed to larger-scale stirring mechanisms captured by single-particle dispersion analyses. Ice beacon triplet arrays have also been used to monitor sea ice deformation off the Canadian east coast and in Antarctica (Prinsenberg et al., 1997; Heil et al., 2002; 2008; 2009; 2011). Studies of correspondence between ice stress, convergence and atmospheric forcing off the southern coast of Labrador in March, 1996 showed little change in convergence within an already compact ice cover, in

addition to an increase in stress with winds and decrease in stress with temperature as the icepack loses its ability to transmit pressure (Prinsenberg et al., 1997). These results are consistent with studies of derived ice motion fields using synthetic aperture radar data showing sea ice deformation and production 1.5 times higher in the seasonal than in the perennial ice zone throughout the Arctic in late fall and winter due to differences in ice strength and thickness (Kwok, 2006).

Application of Lagrangian dispersion (single- and two-particle) in the seasonal ice zone in the Beaufort Sea region in past studies showed that single-particle dispersion captures the existence of two distinct dynamical regimes characterized by distinctive scaling laws; t^2 scaling in the zonal direction characteristic of advection, and $t^{5/4}$ scaling in the meridional direction characteristic of quasi-geostrophic 2D turbulence (Lukovich et al., 2011). Two-particle dispersion studies in this region, based on an assessment of loop and meander reversal events, demonstrated enhanced meridional separation indicative of ice-ice and ice-coast interactions and increased connectivity in the ice cover in winter relative to spring (Lukovich et al., 2014).

In this study we build upon previous analyses to quantify spatiotemporal synoptic changes in sea ice drift and deformation using a novel observational and analytical approach based on one-, two-, and three-particle dispersion statistics. To address the characterization of sea ice drift and deformation using Lagrangian dispersion statistics, we pose the following research questions:

i) How can directional changes in sea ice drift trajectories be characterized? What insight is provided by single-particle dispersion statistics?

ii) How can associated/corresponding sea ice deformation processes for varying distances relative to the coastline be characterized? What insight is provided by two- and three-particle dispersion statistics?

We address these questions through the development of a framework for understanding sea ice drift and deformation in the Beaufort Sea on daily timescales based on single-, two-, and three-particle dispersion. Diagnostic information resulting from this framework can be used by modelers, satellite image analysts and in field observations to quantify relative contributions (atmospheric, oceanic, internal ice stress) to ice drift and the rheological properties of sea ice. Furthermore, these methods are relevant both from an observational and modelling perspective, with the potential for application to

forthcoming model-data comparisons, and an assessment of dynamical regimes in other regions of the Arctic.

The paper proceeds as follows. Data used to identify directional changes in sea ice drift are described in Section 2. In Section 3, methods based on Lagrangian dispersion and the triplet area approach, are presented. Results associated with each of the two objectives are provided in Section 4, followed by conclusions in Section 5 in addition to a short description of future work.

2 Data

Sea ice position data were obtained from an array of ten ice beacons and one ice mass balance buoy launched from the CCGS *Amundsen* in the marginal ice zone of the southern Beaufort Sea in September, 2009 (Figure 1). From this array, four triangular configurations were selected, hereinafter referred to as triplets A to D, to monitor divergence and convergence of sea ice, with initial inter-beacon distances of approximately 11, 11, 11.5, and 7 km for the shortest leg, and 15, 37, 11.5, and 12.5 km for the longest leg, respectively. Triplets A to D were deployed on multi-year ice (MYI) and labeled according to their proximity to the continental coastline: triplet A was located closest to the coastline, while triplet D was located furthest from the coastline. Position coordinates were available for all beacons in: triplet A until October 6th; triplet B until November 4th; triplet C until November 25th, and triplet D until November 3rd, yielding time intervals with durations of 28, 56, 77, and 59 days, respectively. As reported in Lukovich et al. (2011), positional accuracy of the ice beacons ranged from $\delta x = 2.5$ to 5 m based on circular and spherical error probability associated with the GPS module, while temporal accuracy was on the order of nanoseconds and thus negligible. Position accuracy for the ice mass balance buoys was less than 3m according to Garmin GPS16X-HVS product Standard GPS accuracy. The temporal resolution of the beacon data is two hours, and daily averages were calculated for the analysis and time series. Since the anticipated lifetime of the beacon batteries is at least one year, the beacon longevity may be attributed either to alternative mechanical failure or ice deformation and ridging. The data are archived long term through the Canadian Polar Data Catalogue (Buoy triplet centroid 2009 data, 2016).

Sea ice extent and ice type are examined using Environment Canada Canadian Ice Service (CIS) weekly ice charts, in addition to 12.5 km resolution Advanced Microwave Scanning Radiometer – EOS (AMSR-E) daily sea ice concentration (SIC) data. Daily and weekly maps illustrate spatial variability of sea ice concentrations in the Beaufort Sea, while also enabling an assessment of ice conditions in the vicinity of the triplet centroids during their evolution from September to November, 2009.

Atmospheric forcing in the form of sea level pressure (SLP), wind speed and direction, and surface air temperature (SAT) was obtained from North American Regional Reanalysis (NARR) data (Mesinger et al., 2006). Daily atmospheric forcing is derived by averaging 3-hourly NARR data in the vicinity of triplet centroids. Time series of daily-averaged sea level pressure (SLP) are then characterized into relative high (maxima) and low (minima) pressure tendencies. Time series of daily-averaged 10m NARR winds are used to characterize on-shore and off-shore winds.

3 Methods

In this study, single-, two-, and three-particle dispersion statistics are used to quantify dynamical changes in the sea ice cover. Specifically, directional changes in ice drift trajectories are quantified through single-particle dispersion and triplet centroid analyses. Associated deformation processes and differential kinematic parameters (DKPs) are identified through two- and three-particle dispersion. This methodology provides a diagnostic product that quantifies sea ice response to atmospheric forcing (through detection of distinct dynamical regimes in single-particle dispersion), and ice interactions (through identification of deformation and DKPs in two- and three-particle dispersion). Therefore this approach can contribute to topics not specifically addressed since beyond the scope of this study including an understanding of dominant terms in the force balance of sea ice and yielding mechanics associated with DKP component ratios.

In this section we describe the Lagrangian dispersion and triplet centroid approach used to quantify i) directional changes in ice drift trajectories and ii) corresponding sea ice deformation that develops in response to atmospheric forcing for varying distances from the coastline. Presented also are diagnostics (base-to-height and perimeter-to-area ratios, Okubo-Weiss criterion, and shear-to-

divergence ratios) used to characterize sea ice drift and deformation during directional changes in ice drift paths.

3.1 Single-particle dispersion, triplet centroids, and directional changes in ice drift trajectories

Single-particle dispersion monitors organized structure in the flow field and is defined as (Taylor, 1921)

$$A^2 = \langle |x_i(t) - x_i(0) - \langle x_i(t) - x_i(0) \rangle|^2 \rangle$$

for x_i the zonal and meridional location of the ith particle/beacon in the ensemble as a function of elapsed time, t, and where angle brackets denote ensemble averaging. Flow dynamics are characterized by the scaling exponent α according to the relation

$$A^2 \sim t^\alpha,$$

where, $\alpha > 1$ corresponds to a superdiffusive dynamical regime, $\alpha = 1$ to a diffusive regime, and $\alpha < 1$ to a subdiffusive or "trapping" regime. Within the superdiffusive category, $\alpha = 2$ corresponds to a ballistic regime indicative of advection, $\alpha = 5/3$ to an elliptic regime, $\alpha = 5/4$ to a hyperbolic regime. As noted in previous studies, in the context of sea ice dynamics, a ballistic dispersion regime

15 depicts advection associated with organized structure in the ice drift field. An elliptic regime indicates a strong rotational component in the ice drift field, whereas a hyperbolic regime indicates strain (shear and stretching)-dominated flow associated with along-shear transport such as, in this study region, anticyclonic Beaufort Gyre circulation. A diffusive regime captures the behaviour of particles/beacons/ice floes that follow independent random walks (Provenzale, 1999). A subdiffusive

20 regime characterizes trapping such as would occur with dominant contributions from ice-ice-interactions. Previous studies have illustrated the use of Lagrangian dispersion statistics to quantify dynamical regimes in the ice cover (Rampal et al., 2009a,b; Lukovich et al., 2011, 2015; Rampal et al., 2016). In this study, we build upon previous analyses by identifying inflection points in total absolute dispersion results to identify transitions in distinct dynamical regimes.

25   Triplet centroids are calculated from the latitude/longitude coordinates of the three beacons comprising triplets A to D. Directional changes in triplet centroid trajectories on daily timescales are

calculated by applying a three-day running mean to centroid positions, and computing the variance after each mean calculation. The total variance is calculated as the square root of the sum of the squared latitudinal and longitudinal variances. Directional changes are identified according to minima in the total variance time series, capturing interruptions to the ice drift path.

5   Ice and atmospheric conditions are investigated according to the spatial and temporal evolution in ice beacon triplet centroids. Ice drift velocities for each triplet centroid, computed as outlined in Appendix A, further highlight acceleration/deceleration in the triplets during fall, 2009. Turning angles are calculated as the difference between 10 m NARR surface winds and beacon-derived ice drift.

3.2 Two- and three-particle dispersion and sea ice deformation

10   Two-particle dispersion monitors the separation in a pair of particles/beacons/ice floes and is defined as

$$R^2 = \langle (x_i(t) - x_{i+1}(t) - \langle x_i - x_{i+1} \rangle)^2 \rangle$$

for adjacent particle pairs x_i and x_{i+1}, and where angle brackets again denote ensemble averaging. In contrast to single-particle dispersion, two-particle dispersion reflects the behaviour of spatial gradients in the ice drift field rather than the ice drift field itself. Dynamical regimes associated with velocity

15   gradients are defined according to the relation $R^2 \sim t^\beta$. In short- and long-time limits, particles experience linear displacements and approach behaviour comparable to single particles as the pairs lose memory of their origin, respectively. For intermediate times, $R^2 \sim t^3$, in what is referred to as Richardson's (1926) law, resulting from the assumption that eddy diffusivities are dependent on inter-particle separation. In the context of sea ice dynamics, two-particle dispersion characterizes

20   intermittency and heterogeneity in the ice drift field.

In consideration of three-particle dispersion, triplet areas were computed from recorded beacon latitude/longitude coordinates using Heron's formula $A = \sqrt{s(s-a)(s-b)(s-c)}$, where a, b, and c denote the length of the sides for each triplet, and $s = \frac{1}{2}(a + b + c)$. Error propagation analysis for the triangle area and triplet evolution according to Heron's formula yields initial error estimates on the

order of $\delta_A = \frac{\delta x}{\sqrt{8A}}\sqrt{(b^2 + c^2 - a^2)^2 a^2 + (a^2 + c^2 - b^2)^2 b^2 + (a^2 + b^2 - c^2)^2 c^2} \sim 0.05, 0.12, 0.04,$ and 0.04 km^2 for triplets A to D, respectively.

An assessment of the time rate of change in triplet area provides insight about sea ice deformation, namely the differential kinematic parameters (DKPs) of divergence (D), vorticity (V), shearing (S) and
5   stretching (N) deformation rates. In particular, the change in area of a triangular configuration or triplet of drifters to estimate the divergence and local change in flow can be expressed as

$$D = \frac{1}{A}\frac{dA}{dt} = \frac{\partial u}{\partial x} + \frac{\partial v}{\partial y},$$

where A denotes the triangle area, and u and v depict the zonal and meridional components of ocean circulation or ice drift (following Molinari and Kirwan, 1975; LaCasce, 2008; Wadhams, 1989) with negative values corresponding to convergence. Similarly gradients in sea ice motion or deformation
10   characteristics such as vorticity, shearing and stretching deformation rates can be computed from changes in the triplet area through rotation of the velocity vectors (Saucier, 1955). Comparable expressions and their relations are provided both from an oceanic perspective (Saucier, 1955; Molinari and Kirwan, 1975), and in an assessment of sea ice deformation in the Weddell Sea in Wadhams (1989) such that:

$$V = \frac{\partial v}{\partial x} - \frac{\partial u}{\partial y} = \frac{1}{A'}\frac{dA'}{dt}; u' = v \text{ and } v' = -u$$

$$S = \frac{\partial u}{\partial y} + \frac{\partial v}{\partial x} = \frac{1}{A''}\frac{dA''}{dt}; u'' = v \text{ and } v'' = u$$

$$N = \frac{\partial u}{\partial x} - \frac{\partial v}{\partial y} = \frac{1}{A'''}\frac{dA'''}{dt}; u''' = u \text{ and } v''' = -v$$

15   where primes indicate 90° clockwise rotation of velocity vectors. Divergence is associated with a change in area, vorticity with a change in orientation, and shear and stretching with a change in triangle shape due to distortion (Table 2). According to the error estimates for triplet area, a threshold value for significant DKPs relative to uncertainties to ensure a sufficiently large signal to noise ratio is on the order of 10^{-6} s^{-1} for the daily timescales considered.
20   From the perspective of physical changes in sea ice, divergence (convergence) captures opening (closing) in the ice cover related to ice-ocean interactions and flux exchange (ridging). In the Arctic,

negative (positive) vorticity depicts anticyclonic (cyclonic) circulation associated with surface winds and inertial oscillations. Negative (positive) shear captures a shape change whereby the northern triangle beacons travel west (east) relative to the southern pair without changing the triangle area. A negative stretching deformation rate (hereinafter referred to as stretching) indicates stretching along the y-axis (north-south), and shrinking along the x-axis (east-west), without changing the triangle orientation (i.e. stretching parallel or perpendicular to the coast).

In non-divergent flow, the triplet area is conserved so that expansion in one direction is accompanied by contraction in another direction and the triangle becomes an elongated filament (Prinsenberg et al., 1998). Changes in the aspect ratio (defined as the longest leg, or base, divided by the height) also describe changes in the triplet area; i.e., increasing values indicate elongation of the triplet and filamentation or stretching of the triangular configuration, while decreasing values indicate an equilateral configuration. An equilateral triangle is depicted by a base-to-height ratio of $\frac{2}{\sqrt{3}} \sim 1.155$. Furthermore, the perimeter-to-area ratio provides a signature of 'folding' in the sea ice drift cover in a manner similar to mechanical annealing whereby compression reduces the dislocation density of materials (Shan et al., 2007; Lawrence Berkeley National Laboratory, 2008). Perimeter-to-area ratios may also provide insight about floe shape and size distributions (Gherardi and Lagomarsino, 2015). Elongated triangles are captured by vanishing perimeter-to-area ratios, while an equilateral configuration is depicted by a perimeter-to-area ratio of $\sim 4\sqrt{3}/a$, where a is the length of the equilateral triangle side.

Previous studies of DKPs using the triangle area approach have shown that the role of triplet areas in describing DKPs resides in the evolution in the time rate of change in the triangle area (Saucier, 1955; Molinari and Kirwan, 1975). If the lengths of the base (defined as the longest triangle side) and height (defined as the perpendicular distance and 2A/b) differ by an order of magnitude so that the triangle is significantly distorted, a decrease in area will occur. If in addition the change in area exceeds its uncertainty, the DKP associated with the relevant rotation of coordinates will increase, providing a signature of strong deformation. If, however, little change in triplet area is observed (less than the area uncertainty ~ 0.12 km^2), the DKP in question will essentially vanish. In the present study, as is noted below, minimum values for the triplet area amongst all triplets are on the order of 1 km.

Relative contributions of the DKPs are monitored using total deformation $D^2+S^2+N^2$ to assess distortion in the ice cover due to divergence, and the shearing and stretching deformation rates, as well as the vorticity squared V^2 to assess the rotational component (capturing influence from winds and/or inertial oscillations (Gimbert et al, 2012, albeit on shorter timescales)). The Okubo-Weiss (OW) criterion, defined as (Okubo, 1970; Weiss, 1991)

$$OW = Re\left(\frac{1}{4}\left(D^2 + S^2 + N^2 - V^2 + |D|\sqrt{S^2 + N^2 - V^2}\right),\right.$$

highlights relative contributions from deformation and the rotational component. Values with OW < 0 (OW > 0) indicate flow dominated by vorticity (deformation). In order to further distinguish relative contributions from divergence, shearing and stretching deformation rates to the total deformation, the shear to divergence ratio is evaluated such that

$$\theta = arctan\left(\frac{\sqrt{S^2 + N^2}}{D}\right),$$

as a signature of sea ice stress, with implications for rheological characterizations. The shear-to-divergence ratio demonstrates spatial and temporal variability in DKPs and rheological characterizations of the sea ice cover. Values of 0, 45, 90, 135, and 180 degrees depict divergence, extension, shear, contraction, and convergence, respectively (Feltham, 2008; Fossen, 2016).

4 Results and discussion

In this section, we identify directional changes in sea ice drift and corresponding sea ice deformation characteristics using Lagrangian dispersion statistics and additional diagnostics in the context of triplets A to D based on distance from the coastline. Specifically, in the first subsection, single-particle dispersion and factors contributing to identified changes in sea ice drift and dynamical regimes including SLP, surface winds, SAT and sea ice conditions in the vicinity of triplets A to D are investigated. In the second subsection, sea ice deformation is examined using two- and three-particle dispersion.

4.1 Single-particle dispersion and identifying directional changes in sea ice drift

Figure 1. Evolution in Triplet A to D centroid trajectories.

Trajectories for beacons deployed near 135 °W between 72 °N and 75 °N capture spatiotemporal
evolution in ice beacon triplet centroids beginning in September, 2009, with triplet A located closest to,
and triplet D located furthest from, the continental coastline (Figure 1). Triplets A and B, deployed near
72 °N, share two of the three beacons and are advected westwards to approximately 144 °W and 158
°W, surviving until October 7th and November 5th, respectively. Triplet C is deployed near 73 °N and is
also advected westward to 162 °W, surviving until November 26th. Triplet D is deployed near 74.5 °N
and traverses a shorter path southwards and westwards to 145 °W, surviving until November 4th.

From September to November, 2009, eight directional (local) change events are identified based on
changes in the (regional-scale) ice drift path (Figure 1 and Table 1). An initial directional change event
e1 depicts a cusp in all centroid trajectories; a second event *e2* depicts southwestward advection in
triplets A to C and delayed southward migration in Triplet D; a third event *e3* captures southward
migration for all four triplet centroids; *e4* the onset of south and westward migration; *e5* the onset of
south and northwestward migration for all triplet centroids culminating in a loop event for Triplet D
centroid trajectories and following which triplet A stops recording (October 6th); *e6* depicts
northwestward migration in triplets B and C, and a cusp in triplet D; *e7* northwestward migration for all
triplet centroid trajectories; *e8* captures northwestward migration and a loop in triplet C and D centroid
trajectories (Figure 1 and Table 1).

Figure 2. Directional changes in Triplet A to D centroid trajectories

Directional changes in triplet centroid trajectories on daily timescales are, as previously noted,
quantified by time series for total variances of the 3-day running mean triplet centroid positions, and
identified according to minima in these time series (Figure 2). Enhanced latitudinal variance is observed
for Triplet D relative to Triplet A in late September/early October. By contrast longitudinal variance

decreases with increasing distance from the coastline, evidenced in lower values for triplet D relative to triplet A.

Minima in the total variances of the 3-day running mean triplet centroid positions capture directional changes and interruptions in the ice drift field. Maxima also capture departures from the ice drift path. Comparison of SLP highs (Figure 5) and maxima in centroid position variances (Figure 2) demonstrates correspondence between both prior to 8 October during what is described below as the SLP high resulting in Ekman convergence, strong off-shore ice drift, and deterioration in the ice cover. Similar behavior is observed in mean SLP and ice drift triplet centroid variances for all triplets until 8 October, following which SLP and centroid variance maxima are out of phase with a lag of approximately two days.

Figure 3. – Absolute (single-particle) dispersion for all triplets, and regional characterization of sea ice drift.

The loss of synchronicity in ocean-sea ice-atmosphere interactions is further demonstrated in single-particle dispersion statistics for an ensemble including all triplets, providing a regional characterization of sea ice drift in the Southern Beaufort Seas (Figure 3). Specifically, total absolute dispersion is governed by zonal dispersion prior to, and meridional dispersion following, early October, with scaling exponents of $\alpha \sim 3$ and 2, respectively, highlighting a transition in dynamical regimes. Directional change events captured by the (Eulerian) variance interpretation (Figure 2) are also captured by inflection points in the (Lagrangian) single-particle, and most notably, meridional, dispersion analyses (Figure 3).

Figure 4. – Absolute dispersion for beacons comprising triplets, and a local characterization of sea ice drift.

An assessment of local sea ice drift characteristics using single-particle dispersion and a three-beacon ensemble for each centroid demonstrates differences in the ice cover for varying distances from the

coastline (Figures 4a and 4b). Triplets A and B, located closest to the coastline, exhibit considerable meridional variability relative to triplets C and D (upper panel in Figure 4a). Single-particle displacements are also shown to decrease with increasing distance from the coastline. Total absolute dispersion is governed by zonal dispersion (Figure 4a). Furthermore, inflection points in absolute dispersion associated with the local characterization (Figure 4) capture transitions in dynamical regimes due to changes in local ice conditions.

Triplets A and B are characterized by sub-diffusive ($\alpha < 1$) behaviour from 19 September, 2009 to 6 October, 2009, and from 17 – 21, October, 2009, and super-diffusive ($\alpha > 2$) scaling from 7 – 12 October, 2009, and following 22nd October (Figure 4b). Triplet C, located further from the coastline, experiences similar sub-diffusive behaviour prior to 6 October, 2009, and predominantly super-diffusive behaviour following 12 October, 2009. Triplet D, located furthest from the continental coastline experiences the smallest displacements between beacons, with sub-diffusive scaling to 5 October, 2009, and diffusive scaling following 19 October, 2009, with no instances of ballistic scaling. As is explored further below, these dynamical regimes correspond to changes in atmospheric and sea ice conditions.

Figure 5. – Atmospheric forcing and sea ice response – spatial variability

Investigation of atmospheric and sea ice conditions (Figures 5 to 7) shows that mean SLP in the vicinity of triplets A to D is uniform, with some differences in the vicinity of triplet D (Figure 5). By contrast, turning angles highlight spatial variability in ice drift for intervals between high SLP regimes, and provide an initial indication of sea ice mechanics and deformation. Specifically, differences in turning angles highlight spatial (relative to distance from the coastline) differences in sea ice response to external forcing as the SLP high enters the region in the vicinity of the beacon triplets on 8 October, 2009, and subsequent loss of coherence in the ice cover.

Figure 6. – NARR winds, sea ice drift and orientation – spatial variability

Winds and ice drift show coherence in ice drift for triplets A to C, and variations in triplet D (Figure 6). Orientation highlights increased free drift conditions at higher latitudes associated with triplet D relative to lower latitude triplets. Directional changes in sea ice drift occur between SLP high regimes (Figures 2, 3, 5 and 6 and Table 1). In particular, events *e1*, *e3*, *e4*, *e6* and *e8* occur during reversals in wind and ice drift (Figure 6). Noteworthy also are directional changes in sea ice drift during persistent (~3 − 4 days) northerly winds (events *e2*, *e5* and *e7* in Figure 2 and Table 1). Of particular interest is strong offshore ice drift on 8 October due to easterly winds and strong Ekman convergence during a SLP high within a high ice concentration (> 95%) ice regime.

Figure 7. – SIC range and SAT – spatial variability

Surface air temperature (SAT) and sea ice concentrations (SIC) in the vicinity of triplet centroids show that SAT values less than 2 ºC are sustained following 14 September, 2009 for triplets A to D, with an interval of increased SAT near 14 October (Figure 7). SIC varies for triplets A to D, with lower concentrations to 24 September. Low SIC exists during a SLP high for triplet C near 22 September. Lower SICs are observed following the 8 October SLP high indicating deterioration in the sea ice cover.

Figure 8 – Sea ice conditions prior to, during, and following the 8 October SLP high.

An assessment of sea ice and atmospheric conditions shows that the transition in dynamical regimes depicted in the variance time series and absolute dispersion in particular (Figure 3) occurs during a SLP maximum/high, accompanying Ekman convergence and offshore drift. This is further reflected in the poleward retreat in the sea ice edge on 9 and 10 October (Figure 8). In addition, the increase and decrease in meridional displacements during the SLP high for triplets A to D (Figure 3) reflect offshore Ekman drift within a high concentration regime (that suppresses meridional displacements) and subsequent increase in meridional displacements two days following within lower ice concentration regimes indicating failure in the ice cover (Figures 3 and 8). Local ice drift conditions are reflected in subdiffusive scaling (α <1) in total dispersion indicating limited displacements for triplet B within a

high ice concentration regime relative to triplets C and D, where beacons exist within lower ice concentration regimes (Figures 4 and 8) near 19 October.

In summary, results from this section show that single-particle dispersion (namely inflection points in meridional single-particle dispersion statistics) captures directional changes evident in ice drift paths and minima in centroid drift variance, and provides a regional characterization of sea ice drift. Local differences in ice drift at varying distances from the coastline are manifested in absolute dispersion for beacons associated with each triplet. Moreover, absolute dispersion demonstrates a shift in sea ice dynamics during the SLP high on 8 October responsible for convergence in the ice cover, poleward retreat in the ice edge, and strong offshore ice drift.

4.2 Two- and three-particle dispersion and sea ice deformation

Figure 9. Relative (two-particle dispersion).

In this section we explore sea ice drift, and deformation in particular, in the context of two- and three-particle dispersion based on distance relative to the coastline. Relative (two-particle) dispersion shows that total dispersion is initially governed by zonal separation for triplets A, B, and C, and by both zonal and meridional separation for triplet D (Figure 9). This distinction may be attributed to predominantly meridional motion (and along-shear transport) of triplet D along the eastern segment of the anticyclonic Beaufort Gyre. A significant decrease in zonal separation is observed near the ice edge in triplet B due to convergence in the ice cover in response to the SLP high. Inter-beacon distances also increase in the meridional direction and decrease in the zonal direction for triplet B following the SLP high on 8 October. A transition to a more isotropic state in the ice cover for triplets closest to the coastline is evident in comparable zonal and meridional separations in triplets B and C in particular (right panel in Figure 9) following October 27 as beacons encounter lower ice concentrations (Figures 7 and 9).

Whereas events e1, e3, e4, e6, and e8 are associated with reversals in surface winds, changes in along- and across-shear separation accompany northerly winds during events e2, e5, e7, with delayed responses following the SLP high on 8 October. During e2, an increase in along-shear transport is observed for all triplets, with an increase in zonal separations for triplets A, B, and C in the direction of

transport along the southern portion of the anticyclonic Beaufort Gyre, and in meridional separations for triplet D in the direction of motion along the eastern segment of the BG. During e5, an onset in an increase in across-shear transport, namely meridional separation, accompanied by a decrease in zonal separation is observed for triplet B, which is sustained during the SLP high. Following e7, a delayed

5   increase in along-shear transport and zonal separation for all triplets is observed, providing further evidence of loss of synchronicity in ice-atmosphere interactions following the 8 October SLP high. Furthermore, t^3 scaling associated with Richardson's scaling law and attributed to atmospheric dispersion as described in Rampal et al. (2009), is evident ($\beta \sim 3.4$) for triplet C from 10 – 17 October; higher scaling exponents exist for triplets B and D following the SLP high on 8 October.

Figure 10. Triplet area evolution

Figure 11. Evolution in triplet area, base, height, and aspect ratios.

15   Regional differences in triplet area representative of sea ice deformation are observed in the evolution of all triplet triangles (Figure 10). Specifically, triplet area evolution demonstrates enhanced variability in triplet B relative to triplets A, C, and D, with an increase in area near the ice edge in late October/early November (Figure 11). An increase in triangle base (defined as the longest triangle side) is observed with decreasing distance from the coastline (i.e. higher base values for triplets A and B

20   relative to triplets C and D), in a manner consistent with local absolute dispersion (Figure 4). The triplet base also provides a measure of two-particle dispersion and separation between a pair of particles/beacons/ice floes. Triplet area is governed by height. Base-to-height and perimeter to area ratios illustrate an equilateral configuration near the ice edge and coastline in the early stages of evolution for triplet A, and late stages of evolution for triplet B, captured in base-to-height ratio values

25   approaching 1.155. Stretching is observed closest to the coastline following 10 October during a consolidated ice regime (Triplet B), captured in increasing perimeter-to-area and base-to-height ratios.

      As for two-particle dispersion, changes in area, height, and P/A and b/h ratios capture deformation associated with events e2, e5, and e7, with delayed responses to northerly winds following the 8

October SLP high (Figure 11). Following *e2*, the base for triplets A and B increases and height decreases during consolidation, resulting in enhanced P/A and b/h. By contrast, P/A and b/h are approximately constant for triplets C and D, indicating that the triangle maintains its shape further from the continental coastline. Following e5 and the SLP high, the greatest stretching (high base and ratio

5   values) is observed in triplet B located closest to the coastline. Several days following *e7* a decrease in area for triplet B is associated with an decrease in height so that b/h and P/A increase, while once again the area and ratios for triplet C and D remain constant.

Also of interest is enhanced variability in height and area indicating divergence/convergence closer to the coastline, namely for triplet B, following the 8 October SLP high. Triplet C experiences a

10   sustained increase in the triangle base, height, and area following 8 October, in a manner consistent with Gulf of Mexico drifters as described by LaCasce (2008). Referring to a drifter study by LaCasce and Ohlmann (2003), LaCasce (2008) indicated that a sustained increase in triangle area provides a signature of a diffusive regime (such as surface winds) superimposed on ocean dynamics. Triplet D located furthest from the coastline experiences a weak and sustained increase in triangle height and

15   corresponding decrease in aspect ratio. P/A and b/h thus provide a signature of stretching, the relative contributions of which are further described by deformation and DKPs.

Figure 12. Sea ice deformation

20   Local differences in sea ice deformation are further reflected in differential kinematic parameters (DKPs) defined as the weighted time rate of change in triplet area, as described in the methods section (Figure 12). For triplet A, located closest to the coastline, sea ice deformation is characterized predominantly by vorticity and stretching (Figure 12). Triplet B is governed by vorticity for the duration of this triplet evolution, with contributions from shear until 8-10 October, and divergence and stretching

25   following mid-October. Triplet C, located further from the coastline is characterized by vorticity in the early and late stages of triplet evolution with intermittent contributions from shear and to a lesser extent divergence during low ice concentration regimes. Triplet C also experiences enhanced vorticity following the 8 October SLP high. A strong shear event is in addition observed for triplet B during the

SLP high on 8 October, and for triplet C on 10 October. Located furthest from the coastline, triplet D is governed by vorticity, stretching, shear, and divergence in the early stages of development, and by vorticity and to a lesser extent shear for the duration of the triplet evolution. Results further show that sea ice deformation is smallest furthest from the coastline.

5   In consideration of directional changes due to northerly winds e2, e5, and e7, during *e2*, Triplet B experiences a transition from vorticity and stretching to shear, while triplet C is governed by shear. DKPs for triplets A and D are comparatively weak. Similarly during *e5*, weak DKPs are observed for triplet C, with triplets B and D governed by vorticity. During *e7* convergence and divergence dominate for triplet B.

Figure 14. Relative sea ice deformation.

Relative DKPs highlight relative contributions from external forcing associated with winds and bathymetry/distance from the coastline as manifested in vorticity and total deformation, namely the sum

15   of divergence, shear and stretching deformation rates squared. Results show reduced total deformation with increasing distance from the coastline (top panel, Figure 14), particularly following the SLP high on 8 October.   Enhanced vorticity is also observed during low ice concentration regimes, as demonstrated in comparatively high values for triplet D in September, and for triplet B in late October/early November. The Okubo-Weiss criterion provides a signature of deformation- (OW > 0)

20   and vorticity (OW < 0)-dominated regimes. Intervals of divergence and deformation-dominated flow prevail for triplet B, with some instances observed for triplet A, C, and D again in the early stages of evolution. The Okubo-Weiss criterion results in particular show enhanced distortion in the (bounded) ice cover closest to the coastline, especially following the 8 October SLP maximum. Theta values illustrate changes in the ice strength due to relative contributions from divergence and the total strain

25   rate ($S^2 + N^2$). Noteworthy are the high (~180) values during e2, e7, and following e5, indicating convergence associated with offshore ice drift due to Ekman convergence and sea ice deformation associated with along- and across-shear transport.

Previous studies have demonstrated correspondence between ice deformation and stress measurements in the Beaufort Sea (Richter-Menge et al., 2002). Sea ice strength is dependent on ice concentration and thickness. The ice cover fails when the internal ice stress is comparable to ice strength. Results from this analysis suggest that the three-particle dispersion approach, and shear-to-divergence ratio as a measure of ice stress can be used, in combination with ice concentrations and thickness conditions to assess conditions for which failure in the ice cover occurs (Figures 7 and 14). Strong convergence (theta ~ 180) experienced by triplet C on 26 September within a high ice concentration regime, and subsequent reduction in SIC encountered by triplet beacons suggests local failure in the ice cover. In addition, compression experienced by triplet B during the 8 October SLP high and Ekman convergence coincides with reduced ice concentrations and the strong ice shear event (Figures 7, 12, and 14), also indicating failure in the ice cover with non-local effects on triplets C and D. This deterioration further continues near the ice edge for triplet B to 20 October as shear-to-divergence values on order of 180 are accompanied by significant reductions in ice concentrations as the triplet encounters the ice edge and free drift conditions. These results also suggest that directional change events e2 and e7, associated with along-shear transport, northerly surface winds and ice deformation anticipate failure in the ice cover closest to the coastline, although additional study is required to confirm this hypothesis.

Figure 15. Scatter plots of NARR and DKPs: directional changes in response to surface winds and DKPs.

An evaluation of scatter plots showing the number of triplet centroid values in the vicinity of NARR surface winds and associated DKPS highlights sea ice deformation characteristics based on distance from the coastline (Figure 15). Specifically, triplet B is characterized by strong deformation even for low wind speeds, and divergence following the SLP high, indicating dominant contributions from ice-ice interactions closest to the coastline. Deformation for triplet C is accompanied by surface winds on the order of 2 – 5 m/s; events are confined to or characterized by weak divergence and are governed

primarily by shear. Triplet D located furthest from the coastline is characterized by shear at low wind speeds. Most events are associated with weak divergence, negative vorticity, and shear.

In summary, results from this section show that two- and three-particle dispersion capture sea ice deformation associated with directional changes in ice drift paths in response to atmospheric forcing, for varying distances relative to the coastline. Specifically, two- and three-particle dispersion describe sea ice deformation induced by persistent northerly winds (events e2, e5, and e7), enhanced deformation and deterioration in the ice cover following the 8 October SLP high, and regional variations in sea ice deformation, with implications for rheological characterizations of sea ice.

6 Conclusions

In this study we developed a framework to characterize directional changes in sea ice drift and associated deformation processes in response to atmospheric forcing based on Lagrangian dispersion statistics. We tested this approach using single-, two-, and three-particle dispersion applied to beacon arrays deployed in a triangular configuration as triplets at varying distances from the coastline in the southern Beaufort Sea.

In consideration of our first research question, single-particle dispersion characterizes directional changes in sea ice drift trajectories and dynamical changes in the ice cover. Specifically, single-particle dispersion captures i) a shift in ice dynamical regimes following the 8 October SLP high, ii) inflection points and directional changes in the meridional ice drift component associated with interactions with the coastline, and iii) loss of synchronicity in ice-atmosphere interactions to provide a regional characterization of sea ice drift. Local differences in scaling and ice drift at varying distances from the coastline are captured by single-particle dispersion for beacons associated with each triplet. Single-particle displacements are also shown to decrease with increasing distance from the coastline.

In consideration of our second research question, two- and three-particle dispersion characterize associated deformation processes for varying distances relative to the coastline. In particular, two- and three-particle dispersion capture i) sea ice deformation induced by northerly winds and accompanying along- and cross-shear transport ii) relative DKPs and enhanced deformation with decreasing distance from the coastline following the 8 October event, and iii) local and regional variations in sea ice

deformation in the ice cover relevant for rheological characterizations of sea ice based on an assessment of the shear-to-divergence ratios.

In terms of impacts and insight addressed in the discussion, Lagrangian dispersion thus provides a framework and prescription for understanding directional changes in sea ice drift and accompanying deformation in response to atmospheric forcing. The diagnostics and tools developed in this study provide a unique characterization of sea ice drift and deformation processes in the southern Beaufort Sea, with implications for ice hazard assessments and forecasting applications. Results from this analysis can be applied to develop an integrated observational-modeling framework for Lagrangian dispersion designed specifically to understand ice-atmosphere interactions in the context of drift and deformation at regional and local spatial scales. Building on diagnostics and insights from this study, new techniques to examine higher-frequency fluctuations associated with inertial oscillations are explored in a companion paper (Geiger and Lukovich, in preparation). Implications for EVP and rheological characterizations of sea ice using observations, results and diagnostics from this investigation could further be explored.

Proposed work using results from this study includes efforts to address the question: What are the implications of changing ice and atmospheric patterns and dynamics for ice –atmosphere interactions, including heat and momentum exchange in particular, and local and global-scale processes more generally? Answering this question using diagnostics that evaluate underlying structure in atmospheric, sea ice and oceanographic flow fields will be essential in/contribute to understanding, predicting, and addressing climate change impacts within an increasingly unpredictable environmental regime.

Acknowledgements

Buoy data were funded by the Natural Sciences and Engineering Research Council of Canada, the Canada Foundation for Innovation and partner organizations. Funding for this study was also provided by the Canadian Networks of Centres of Excellence (NCE) program, and Canada Research Chairs (CRC) programme (D.G. Barber). The authors would like to thank D. Babb and R. Galley for triplet deployment and for contributions to an earlier version of this manuscript. This work was completed as a contribution to the ArcticNet and Arctic Science Partnership networks.

References

Bouillon, S. and Rampal, P.: On producing sea ice deformation data sets from SAR-derived sea ice motion, The Cryosphere, 9, 663-673, doi:10.5194/tc-9-663-2015, 2015.

5   Barber, D. G., Galley, R., Asplin, M.G., De Abreu, R., Warner K.-A., Pućko, M., Gupta, M., Prinsenberg S., Julien, S.: Perennial pack ice in the southern Beaufort Sea was not as it appeared in the summer of 2009, Geophys. Res. Lett., 36, L24501, doi:10.1029/2009GL041434, 2009.

Bourassa, M. A., Gille, S. T., Bitz, C., Carlson, D., Clayson, C. A., Cerovecki, I., Cronin, M. F.,
10   Drennan, W. M., Fairall, C. W., Hoffman, R. N., Magnusdottir, G., Pinker, R. T., Renfrew, I. A., Serreze, M., Speer, K., Talley, L. D., and Wick, G. A.: High-latitude ocean and sea ice surface fluxes: Challenges for climate research. Bulletin of the American Meteorological Society, 94, 3, 403-423, 2013.

Carleton, A. M.: Synoptic sea ice-atmosphere interactions in the Chukchi and Beaufort Seas from
15   NIMBUS 5 ESMR data, J. Geophys. Res., 89, D5, 7245–7258, doi:10.1029/JD089iD05p07245, 1984.

Carmack, E., Polyakov, I., Padman, L., Fer, I., Hunke, E., Hutchings, J., Jackson, J., Kelley, D., Kwok, R., Layton, C., Melling, H., Perovich, D., Persson, O., Ruddick, B., Timmermans, M.-L., Toole, J., Ross, T., Vavrus, S., and Winsor, P.: Toward quantifying the increasing role of oceanic heat in sea ice
20   loss in the new Arctic, Bulletin of the American Meteorological Society, 96,12, 2079-2105, 2015.

Colony, R. and Thorndike, A.S.: An estimate of the mean field of Arctic sea ice motion, J. Geophys. Res., 89, C6, 10,623–10,629, doi:10.1029/JC089iC06p10623, 1984.

25   Colony, R. and Thorndike, A.S.: Sea ice motion as a drunkard's walk, J. Geophys. Res., 90, C1, 965–974, doi:10.1029/JC090iC01p00965, 1985.

Geiger, C.A., Ackley, S.F., and Hibler III, W.D.: Sea ice drift and deformation processes in the western Weddell Sea, in *Antarctic Sea Ice: Physical Processes, Interactions and Variability*, Antarct. Res. Set.,
30   vol. 7, pp. 141-160, edited by M.O. Jeffries, AGU, Washington, D.C., 1998.

Geiger, C.A., Zhao, Y., Liu, A.K., and Hakkinen, S.: Large-scale comparison between buoy and SSM/I drift and deformation in the Eurasian Basin during winter, 1992 – 1993, J. Geophys. Res., 105, C2, 2257 – 3368, 2000.
35
Geiger, C.A. and Drinkwater, M.R.: Impact of temporal-spatio resolution on sea-ice drift and deformation, IUTAM Symposium on Scaling Laws in Ice Mechanics and Dynamics, (eds.) J.P. Dempsey and H.H. Shen, Kluwer Academic Publishers, Netherlands, 407-416, 2001.

40   Geiger, C. A. and Perovich, D.K.: Springtime ice motion in the western Antarctic Peninsula region, Deep-Sea Res. II, 55, 338 – 50, 2008.

Gherardi, M. and Lagomarsino, M.C.: Characterizing the size and shape of sea ice floes, Nature, Scientific Reports 5, 10226, doi: 10.1038/srep10226, 2015.

5   Guest P. S. and Davidson, K.L.: The aerodynamic roughness of different types of sea ice. J. Geophys. Res. 96, C3, 4709–4721, 1991.

Hakkinen, S.: Coupled ice–ocean dynamics in the marginal ice zones: upwelling/downwelling and eddy generation. J.Geophys. Res. 91, C1, 819–832, 1986.

Hakkinen, S., Proshutinsky, A., Ashik, I.: Sea ice drift in the Arctic since the 1950s, Geophys. Res. Lett., 35, L19704, doi:10.1029/2008GL034791, 2008.

Heil, P. and Hibler, W.D.: Modeling the high-frequency component of Arctic sea ice drift and
15   deformation, J. Phys. Oceanography, 32, 3039 – 3057, 2002.

Heil, P., Hutchings, J.K., Worby, A.P., Johansson, M., Launiainen, J., Haas, C., and Hibler, W.D.: Tidal forcing on sea-ice drift and deformation in the western Weddell Sea in early austral summer, 2004, Deep-Sea Res., Part II – Topical studies in oceanography, 55, 8-9, 943-962, 2008.

Heil, P., Massom, R.A., Allison, I., Worby, A.P., and Lytle, V.I.: Role of off-shelf to on-shelf transitions for East Antarctic sea ice dynamics during spring 2003, J. Geophys. Res. – Oceans, 114, C09010, doi:10.1029/2008JC004873, 2009.

25   Heil, P., Massom, R.A., Allison, I., Worby, A.P.: Physical attributes of sea-ice kinematics during spring 2007 off East Antarctica, Deep-Sea Res., Part II- Topical studies in oceanography, 58, 9-10, 1158 – 1171, 2011.

Hutchings, J. K., Heil, P., Hibler III, W. D.: On modelling linear kinematic features in sea ice. Monthly
30   Weather Review, 12, 3481-3497, 2005.

Hutchings, J.K., Roberts, A., Geiger, C., and Richter-Menge, J.: Spatial and temporal characterization of sea-ice deformation, Ann. Glaciol., 52,57 Pt 2, 360–368, doi: 10.3189/2011AoG57A185, 2011.

35   Hwang, P. A.: Temporal and spatial variation of the drag coefficient of a developing sea under steady wind-forcing. J. Geophys. Res., 110, C07024, doi:10.1029/2005JC002912, 2005.

Kwok, R., Contrasts in sea ice deformation and production in the Arctic seasonal and perennial ice zones, J. Geophys. Res., 111, C11S22, doi:10.1029/2005JC003246, 2006.

Kwok, R. and Cunningham, G. F.: Deformation of the Arctic Ocean ice cover after the 2007 record minimum in summer ice extent, CRST, 76-77, doi: 10.1016/j.coldregions.2011.04.003, 2012.

LaCasce, J.H.: Lagrangian statistics from oceanic and atmospheric observations, Lect. Notes Phys., 744, 165-218, 2008.

5 Lawrence Berkeley National Laboratory (2008, January 3), Mechanical Annealing, Increased Strength and Why Materials Get Stronger as They Get Smaller. Retrieved from http://www.azonano.com/article.aspx?ArticleID=2045.

LeDrew, E.F., Johnson, D., Maslanik, J.A.: An examination of atmospheric mechanisms that may be 10 responsible for the annual reversal of the Beaufort Sea ice field. Int. J. Clim. 11, 841–859, 1991.

Lukovich, J., Geiger, C.A., Babb, D., Galley, R., and Barber, D.G.: Ice beacon triplet deployments in the Beaufort Sea gyre, 2009 Arctic Net Ice Beacon GPS Positions and Centroid Triplet Arrays, Centre for Earth Observation Science, Canadian Cryospheric Information Network Reference Number 12709, 15 Polar Data Catalogue, 2016.

Lukovich, J.V., Babb, D.G., and Barber, D.G.: Ice beacon trajectories in the Arctic during the IPY-CFL study, J. Geophys. Res., doi:10.1029/2011JC007049, 2011.

20 Lukovich, J.V., Belanger, C., Barber, D.G., and Gratton, Y.: On coherent ice drift features in the Beaufort Sea gyre, *Deep Sea Res*., Part I: Oceanographic Research Papers, 92, 56 – 74, 2014.

Lukovich, J.V., Hutchings, J.K., and Barber, D.G.: On sea ice dynamical regimes in the Arctic Ocean, *Annals of Glaciology*, 56, 69, 323 – 331, 2015.
25
McPhee, M.G.: Advances in understanding ice–ocean stress during and since AIDJEX, Cold Regions Science and Technology, Volumes 76–77, 24-36, http://dx.doi.org/10.1016/j.coldregions.2011.05.001, 2012.

30 Mesinger, F., DiMego, G., Kalnay, E., Mitchell, K., Shafran, P.C., Ebisuzaki, W., Jovic, D., Woollen, J., Rogers, E., Berbery, E.H., Ek, M.B., Fan, Y., Grumbine, R., Higgins, W., Li, H., Lin, Y., Manikin, G., Parrish, D., and Shi, W.: North American regional reanalysis, Bulletin of the American Meteorological Society, 87, 3, 343 – 360, 2006.

35 Molinari, R. and Kirwan, A.D.: Calculations of differential kinematic properties from Lagrangian observations in western Caribbean Sea, J. Physical Oceanography, 5, 3, 483-491, 1975.

Okubo, A.: Horizontal dispersion of floatable particles in the vicinity of velocity singularities such as convergences, Deep Sea Res., 17, 445–454, 1970.
40
Overland, J., Walter, B., Curtin, T. B., and Turet, P.: Hierarchy and sea ice mechanics: A case study from the Beaufort Sea, J. Geophys. Res., 100, C3, 4559 – 4571, 1995

Polar Group, The: Polar atmosphere-ice-ocean processes: A review of polar problems in climate research, Rev. Geophys.,18, 2, 525–543, doi:10.1029/RG018i002p00525, 1980.

5   Preller, R. B., and Posey, P.G.: A numerical model simulation of a summer reversal of the Beaufort Gyre, Geophys. Res. Lett., 16, 69– 72, 1989

Prinsenberg, S.J., Fowler, G.A., van der Baaren, A.: Pack ice convergence measurements by GPS-ARGOS ice beacons, Cold Regions Science and Technology, 28, 2, 59-72, doi: 10.1016/S0165-
10   232X(98)00013-5, 1998.

Proshutinsky, A., Dukhovskov, D., Timmermans, M.-L., Krishfield, R., Bamber, J.L.: Arctic circulation regimes, Phil. Trans. R. Soc. A, 373, 1 – 18, doi:10.1098/rsta.2014.0160, 2015.

15   Rampal, P., Weiss, J., Marsan, D., Lindsay, R., and Stern, H.: Scaling properties of sea ice deformation from buoy dispersion analysis, J. Geophys. Res., 113, C03002, doi:10.1029/2007JC004143, 2008.

Rampal, P., Weiss, J., Marsan, D., and Bourgoin, M.: Arctic sea ice velocity field: General circulation and turbulent-like fluctuations, J. Geophys. Res., 114, C10014, doi:10.1029/2008JC005227, 2009a.
20
Rampal, P., Weiss, J., and Marsan, D.: Positive trend in the mean speed and deformation rate of Arctic sea ice, 1979–2007, J. Geophys. Res., 114, C05013, doi:10.1029/2008JC005066, 2009b.

Rampal, P., Bouillon, S., Bergh, J., and Ólason, E.: Arctic sea-ice diffusion from observed and
25   simulated Lagrangian trajectories, The Cryosphere, 10, 1513-1527, doi:10.5194/tc-10-1513-2016, 2016.

Richter-Menge, J. A., McNutt, S. L., Overland, J. E., and Kwok, R.: Relating Arctic pack ice stress and deformation under winter conditions, J. Geophys. Res., 107, C10, 8040, doi:10.1029/2000JC000477, 2002.
30
Saucier, W.J.: Principles of meteorological analysis, University of Chicago Press, Chicago, IL, 438 pp., 1955.

Shan, Z.W., Mishra, R.K., Sayed Asif, S.A., Warren, O.L., Minor, A.M.: Mechanical annealing and
35   source-limited deformation in submicrometre-diameter Ni crystals, Nature Materials 7, 115 – 119, 2007.

Spreen, G., Kwok, R., Menemenlis, D.: Trends in Arctic sea ice drift and role of wind forcing: 1992– 2009. Geophys. Res. Lett. 38, L19501, http://dx.doi.org/10.1029/2011GL048970, 2011.
40
Stern H.L. and Lindsay, R.W.: Spatial scaling of Arctic sea ice deformation. J. Geophys. Res., 114, C10, C10017, doi:10.1029/2009JC005380a, 2009.

Stroeve J., Serreze M, Drobot S, Gearheard S, Holland M, Maslanik J, Meier W, and Scambos T.: Arctic sea ice extent plummets in 2007. EOS, Trans. Am. Geophys. Union 89, 13–14, doi:10.1029/2008EO020001), 2008.

Taylor, G. I.: Diffusion by continuous movements, Proc. London Math. Soc., s2-20, 196–212, doi:10.1112/plms/s2-20.1.196, 1921.

Thorndike, A. S.: Kinematics of sea ice, The Geophysics of Sea Ice, NATO ASI Ser., Ser. B, 146N. Untersteiner, Plenum, New York., 489–549, 1986.

Wadhams et al.: Basin-scale ice motion and deformation in the Weddell Sea in winter, Annals of Glaciology, 12, 178 – 186, 1989.

Weiss, J.: The dynamics of enstrophy transfer in two-dimensional hydrodynamics, Physica D, 48, 273–294, 1991.

Weiss, J.: Drift, deformation, and fracture of sea ice, Springer Briefs in Earth Sciences, Springer Netherlands, Dordrecht Netherlands, doi:10.1007/978-94-007-6202-2 5, 2013.

Weiss J, Dansereau V.: Linking scales in sea ice mechanics. Phil. Trans. R. Soc. A 375: 20150352, 2017.
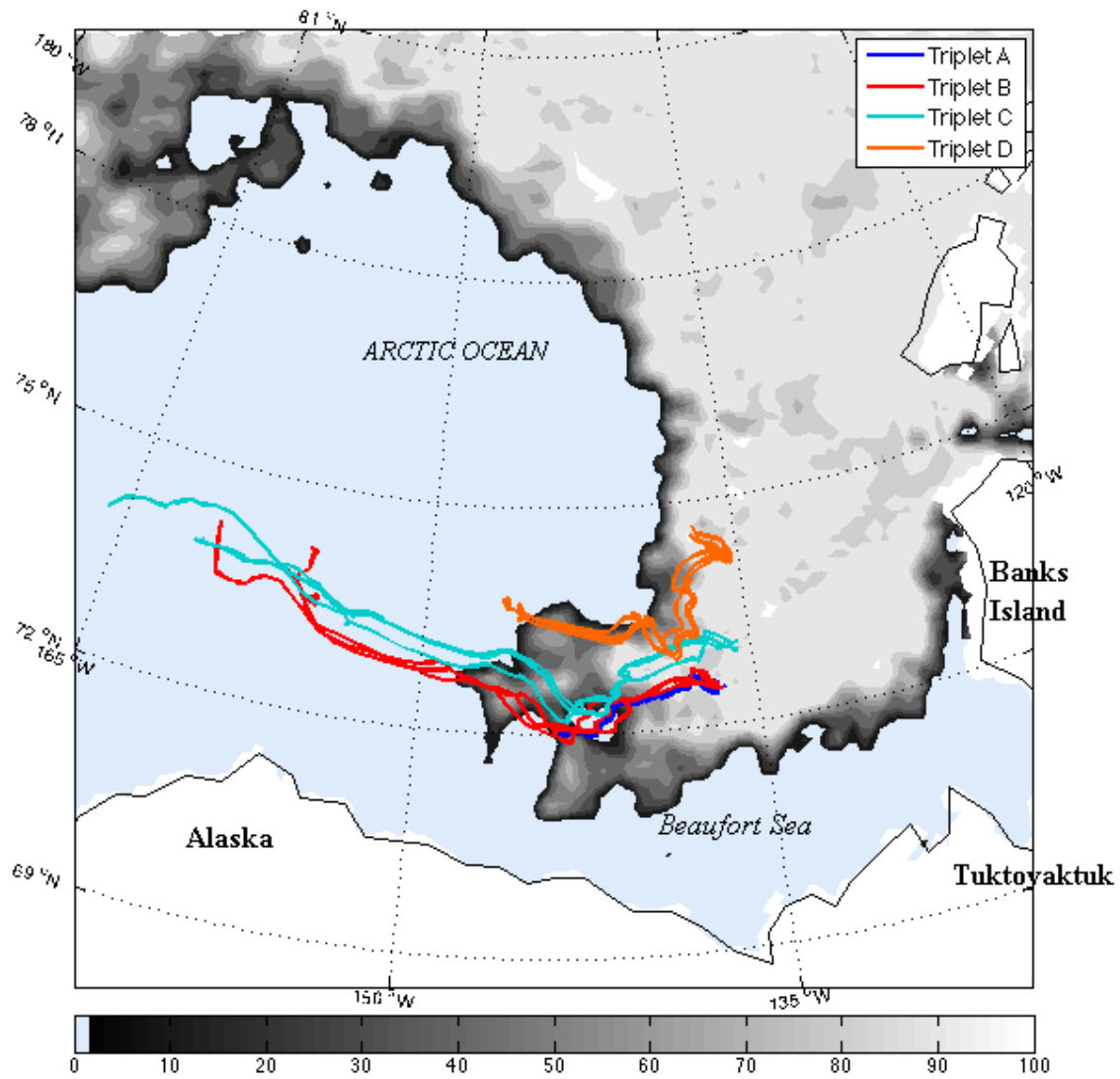
Figure 1a: GPS buoy-array-triplet trajectories relative to sea ice and coastline. Evolution in triplet A to D centroid trajectories, superimposed on sea ice concentration map in early September, 2009 on triplet deployment, with triplet A located closest to the coastline, and triplet D located furthest from the coastline. Triplet D is also initially located nearest the tongue of multiyear ice edge.
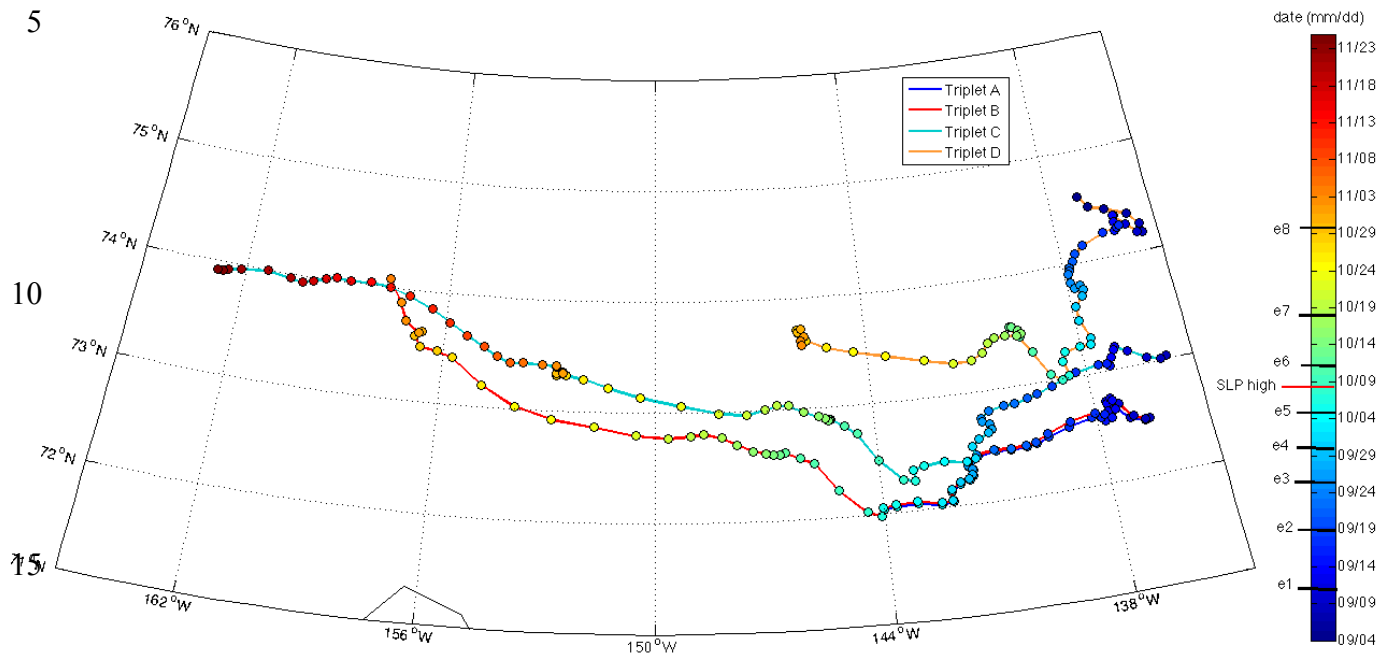
20   **Figure 1b: Temporal evolution of triplet centroids A to D, colour-coded by date with each directional change event enumerated in the colourbar timeline. The SLP high resulting in strong offshore ice drift, and decoupling in ice-atmosphere interactions is also depicted.**
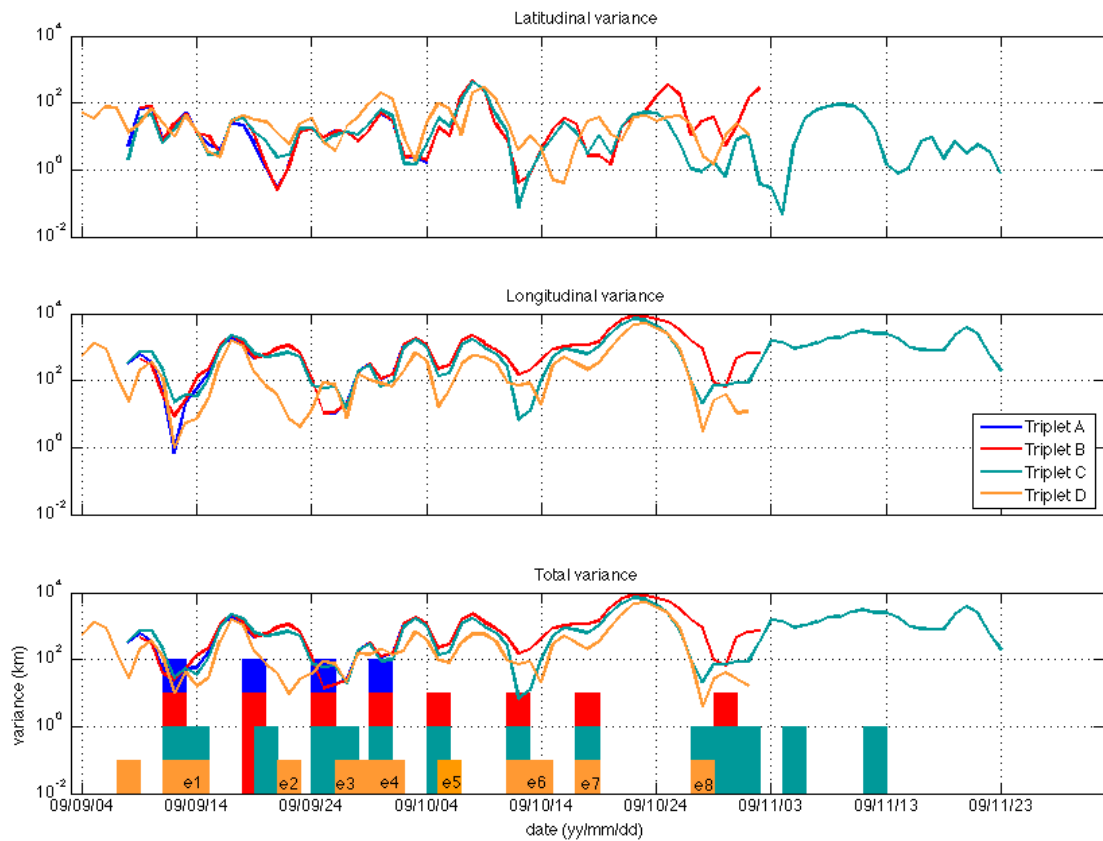
Figure 2: Directional changes in triplet A to D centroid trajectories, defined as minima in the variances of the 3-day running mean triplet centroid positions. The upper, middle, and lower panels depict latitudinal, longitudinal and total variance, respectively. Comparison with mean SLP in the vicinity of the triplets shows correspondence between SLP and drift variance maxima prior to 8 October; minima occur between SLP and variance maxima.
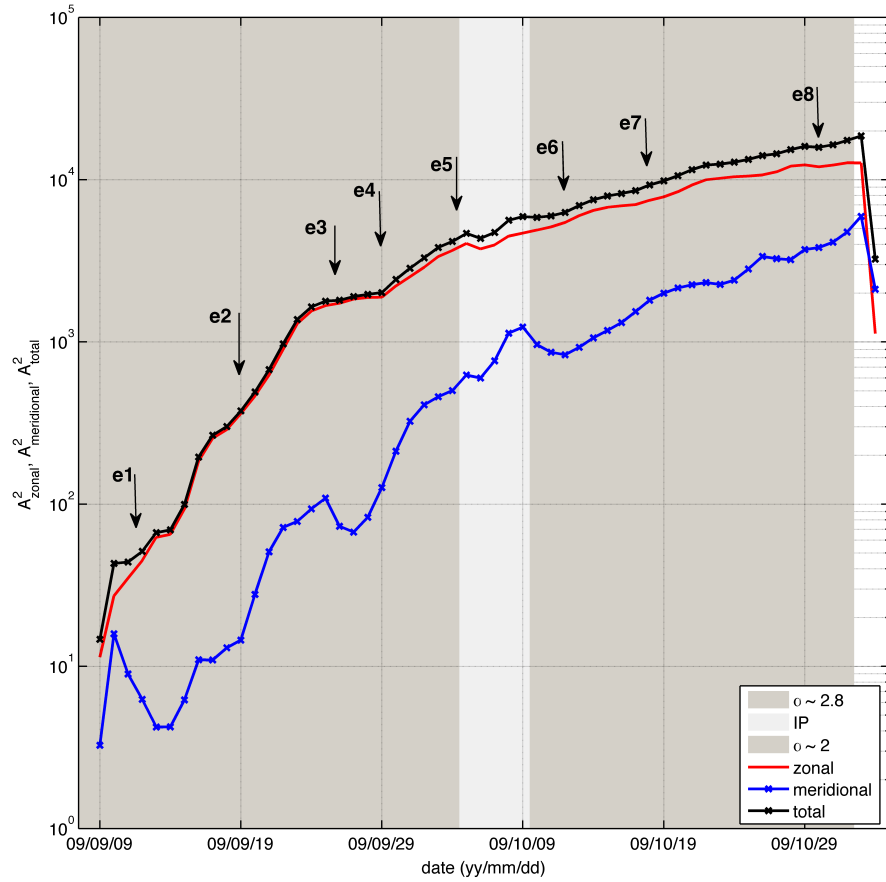
Figure 3: Absolute (single-particle) dispersion statistics for triplets A to D, depicting zonal (red), meridional (blue), and total (black) dispersion. Light shaded area depicts inflection point (IP) range, and dark shaded areas dynamical regimes associated with α ~ 3 and α ~ 2 prior to and following the inflection point range, capturing increased contributions from meridional drift. Arrows and labels depict triplet events derived from the variance analysis.
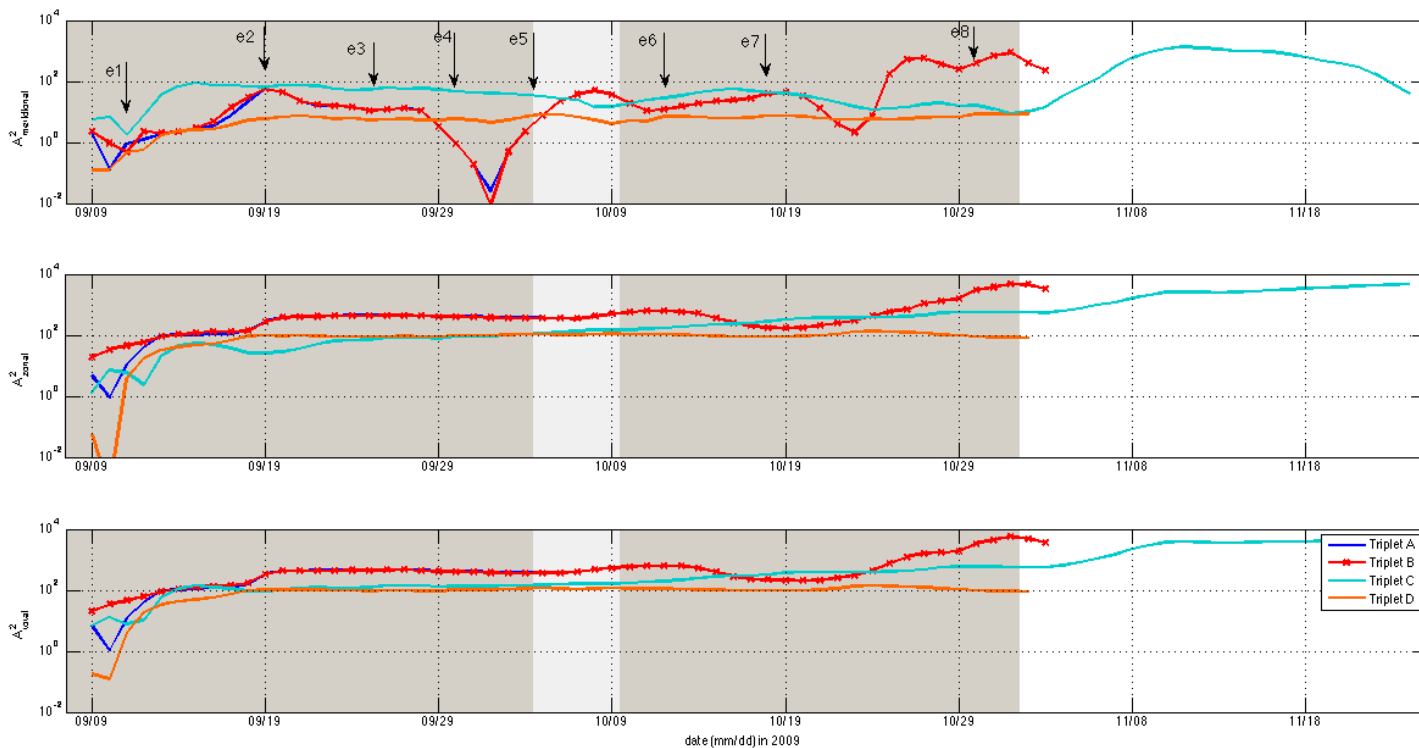
Figure 4a: Absolute (single-particle) dispersion statistics depicting meridional (top), zonal (middle), and total (lower) dispersion for beacons comprising triplets A (blue), B (red), C (cyan) and D (amber), to characterize local changes in ice drift at varying distances from the coastline. Shading and arrows are as in Figure 3 providing a regional characterization.
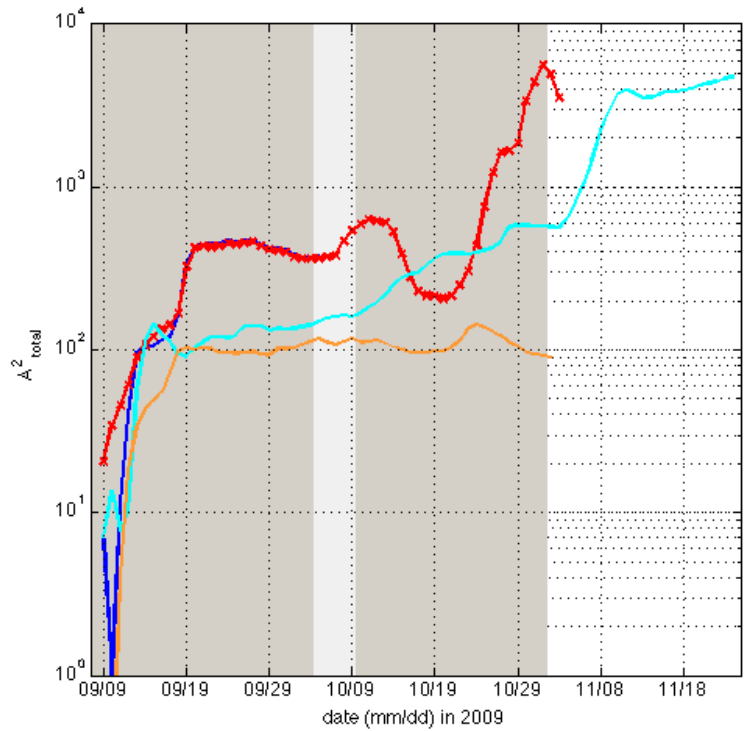
Figure 4b: Total single-particle dispersion for triplets A (blue), B (red), C (cyan), and D (amber) as an enlargement of lower panel in Figure 4a, capturing temporal evolution in and differences between triplet slopes based on local beacon behaviour associated with each triplet.
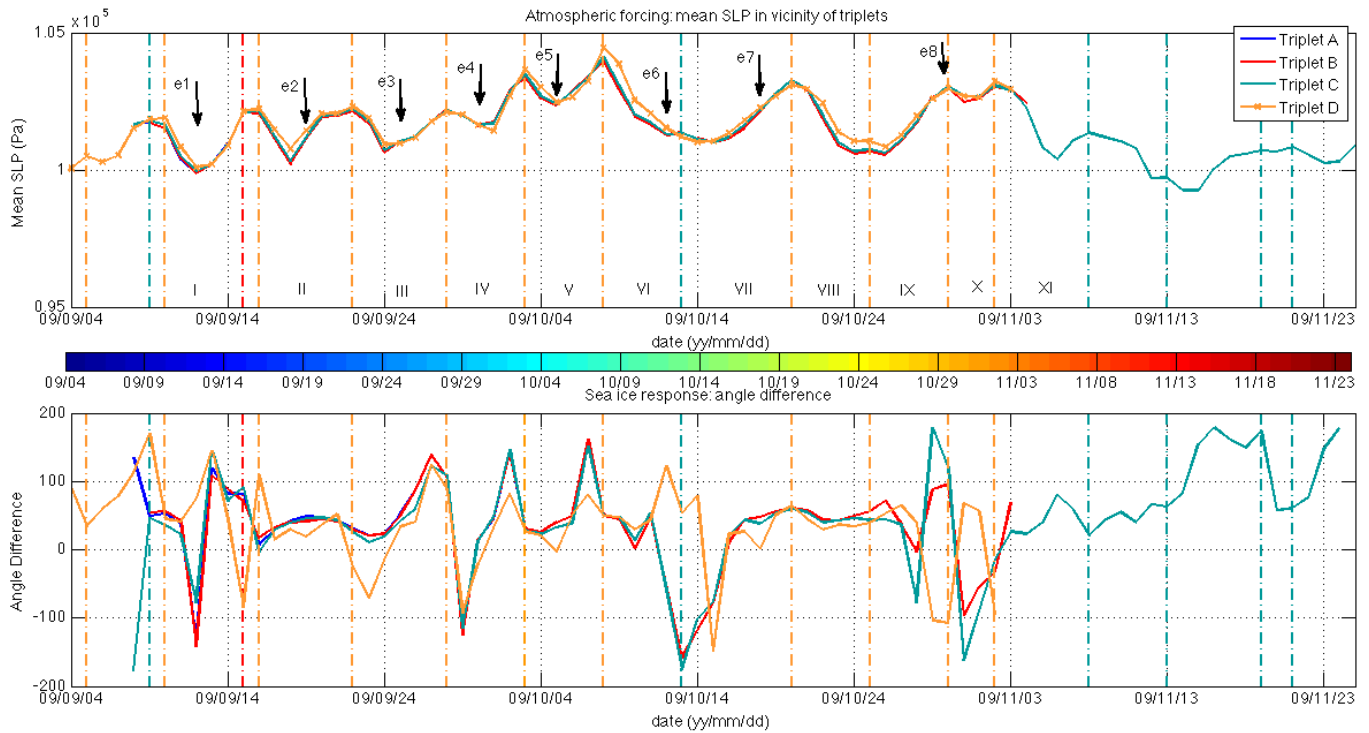
Figure 5: Atmospheric forcing and regional sea ice response. Mean SLP in the vicinity of triplets A to D highlighting atmospheric
10 **forcing (upper panel). Turning angle between surface winds and triplet centroid drift depicting sea ice response (lower panel).**
Colour bar indicates colours associated with centroid dates in Figure 1b.
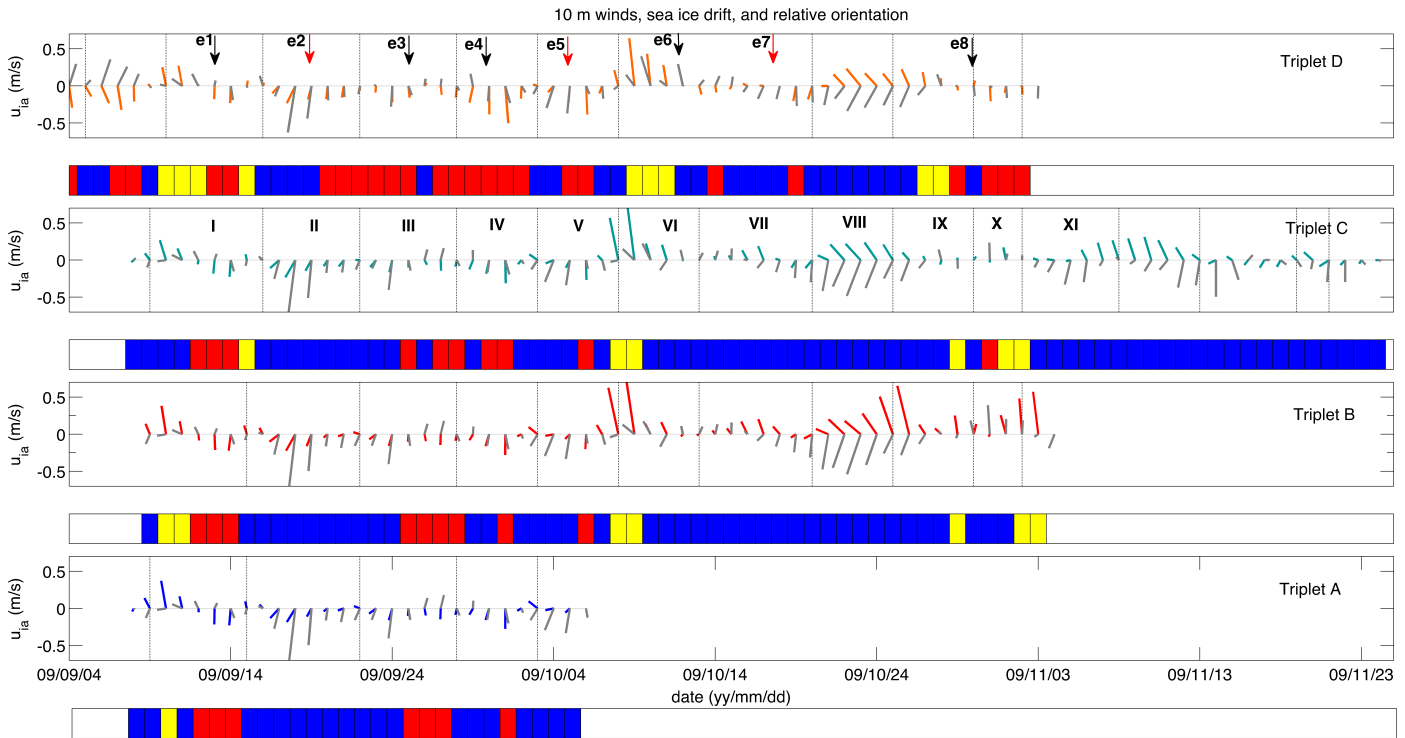
Figure 6: Winds, sea ice drift and orientation relative to the coastline. Time series of 10 m North American Regional Reanalysis (NARR) winds in the vicinity of the triplet centroids (grey vectors), sea ice drift for triplets A (lowermost panel) to D (uppermost panel), and offshore (yellow), onshore (red), and alongshore (blue) ice drift orientation.
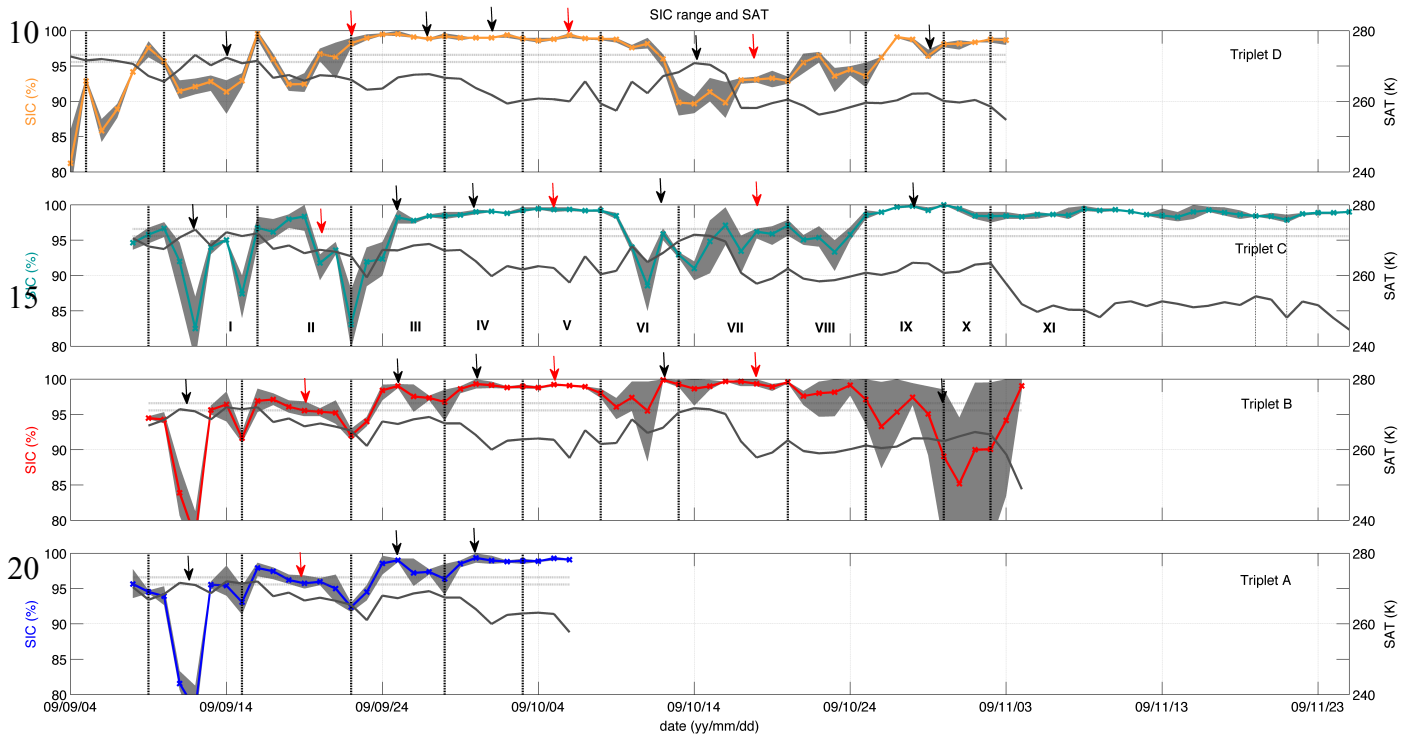
Figure 7: Sea ice concentration (SIC) range and Surface Air Temperatures (SAT). Time series of percent sea ice concentration and SAT for triplets A (lowermost panel) to D (uppermost panel). Vertical lines depict dates associated with SLP highs and roman numerals the SLP interval described in Table 3. Grey shading shows the range of ice concentrations encountered by three beacons comprising the triplets. Horizontal lines depict SAT values of 273 K and 275 K.
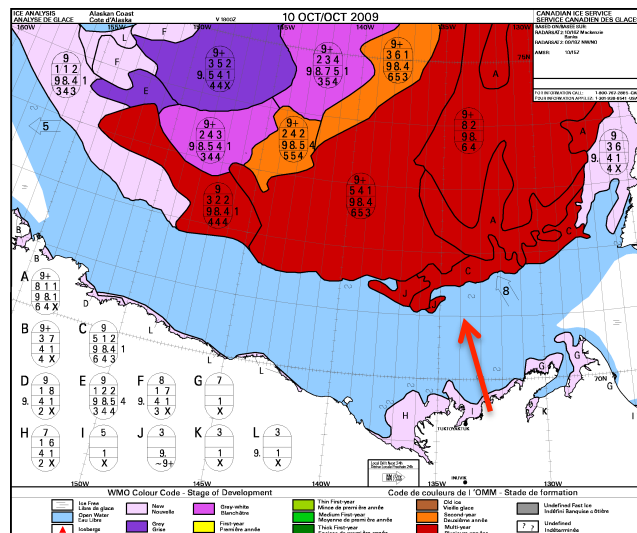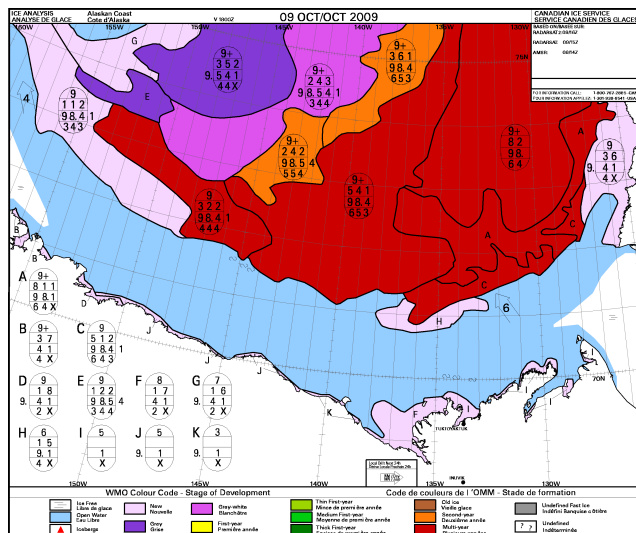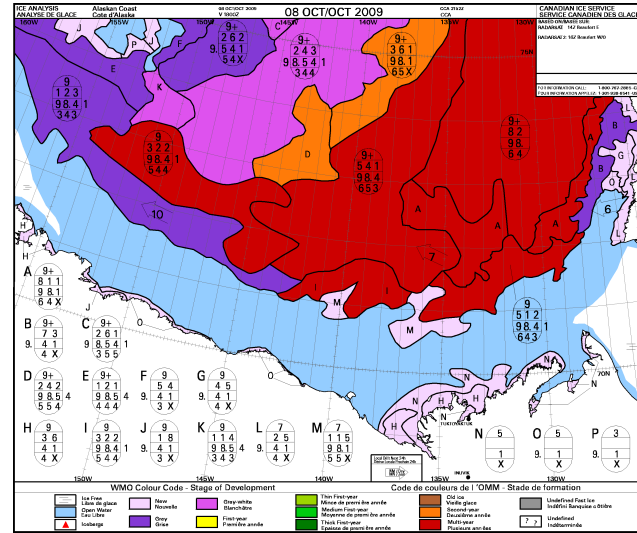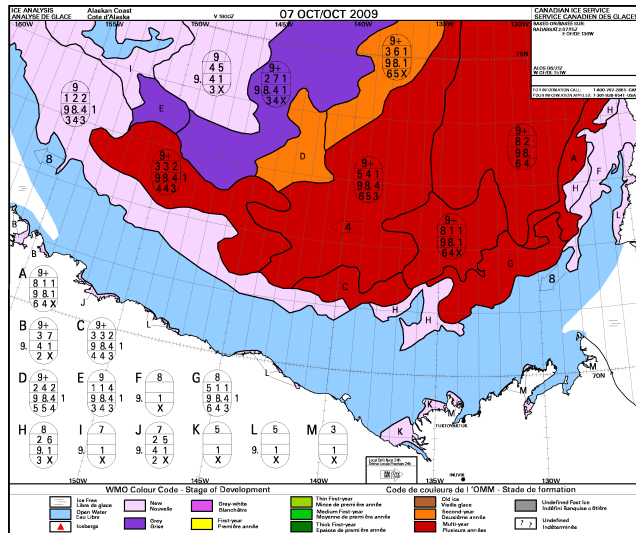
Figure 8: Canadian Ice Service ice charts showing sea ice development stages on 7, 8, 9, and 10 October prior to, during, and following the 8 October SLP high. Noteworthy is the poleward retreat in the ice edge on 10 October due to sea ice convergence associated with the SLP high.
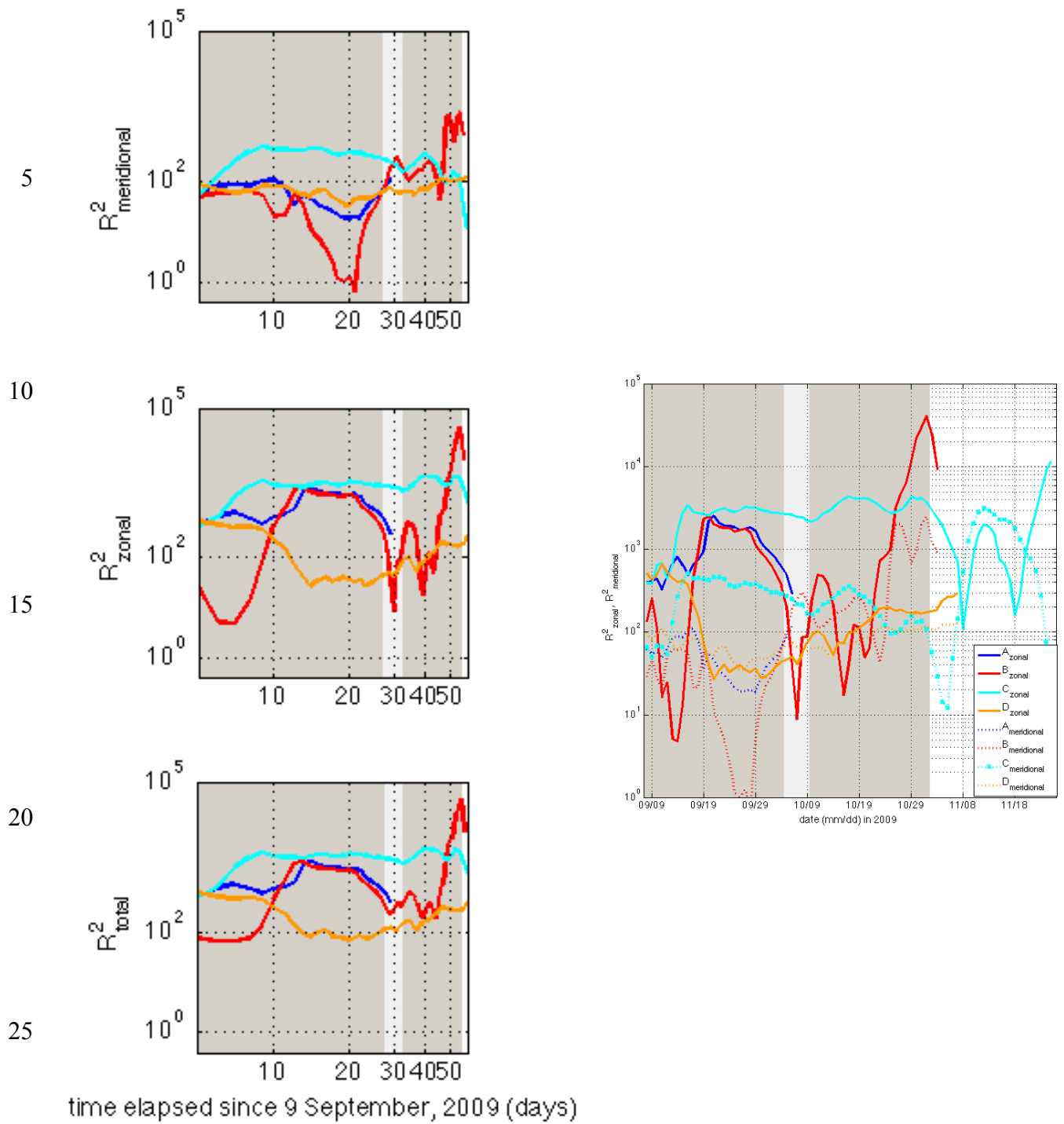
Figure 9 Relative (two-particle) dispersion showing (left column) meridional (top), zonal (middle), and total (lower panel) relative dispersion as a function of elapsed time since 9 September, 2009, and (right panel) a superposition of zonal (solid line) and meridional (symbol dashed line) relative dispersion.
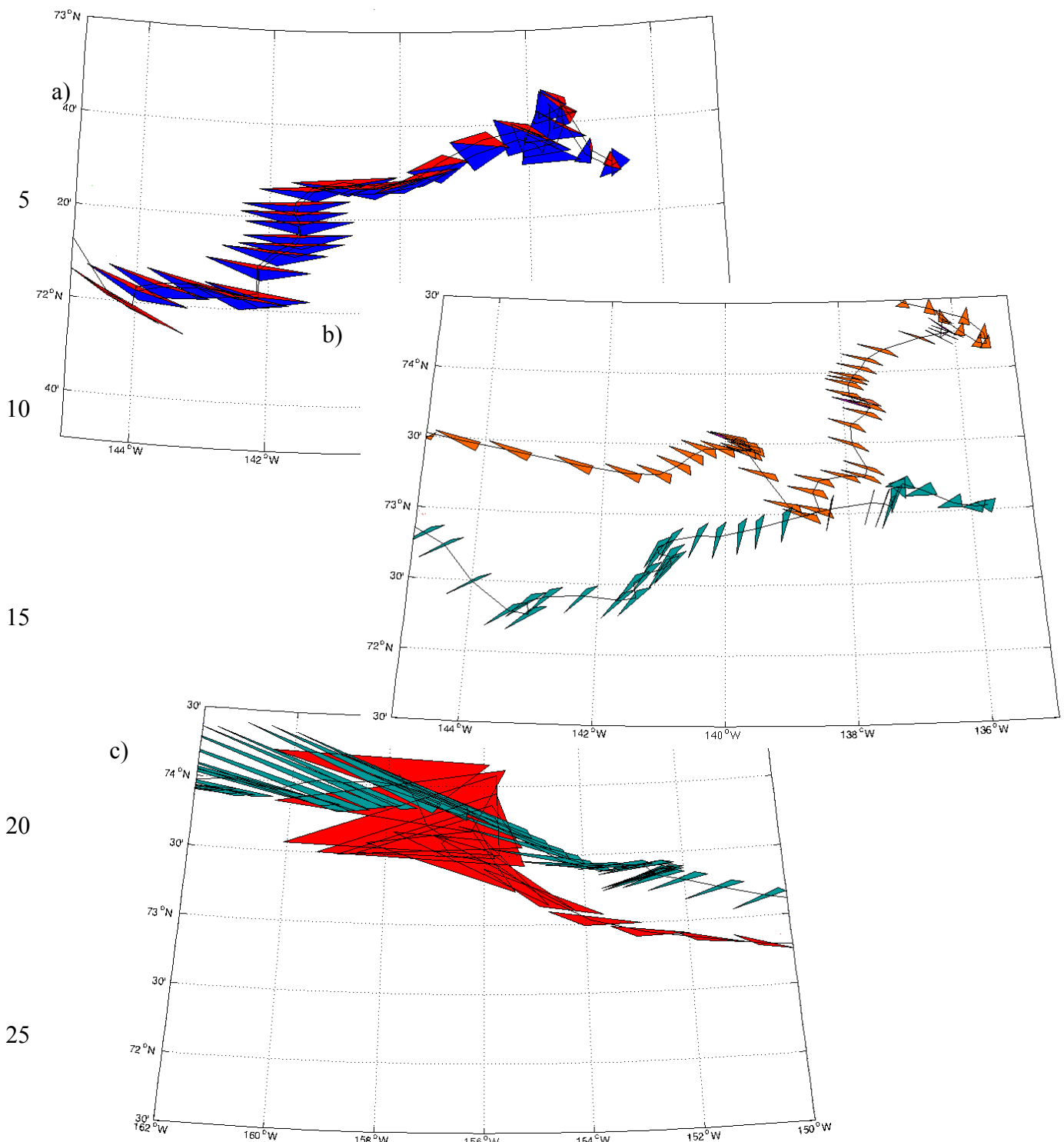
Figure 10: Triplet area evolution. Examples of triplet evolution for triplet A (blue triangle), B (red triangle), C (cyan triangle), and D (amber triangle), including (a) initial evolution in triplets A and B, (b) evolution in triplets C and D, (c) final evolution in triplets B and C.
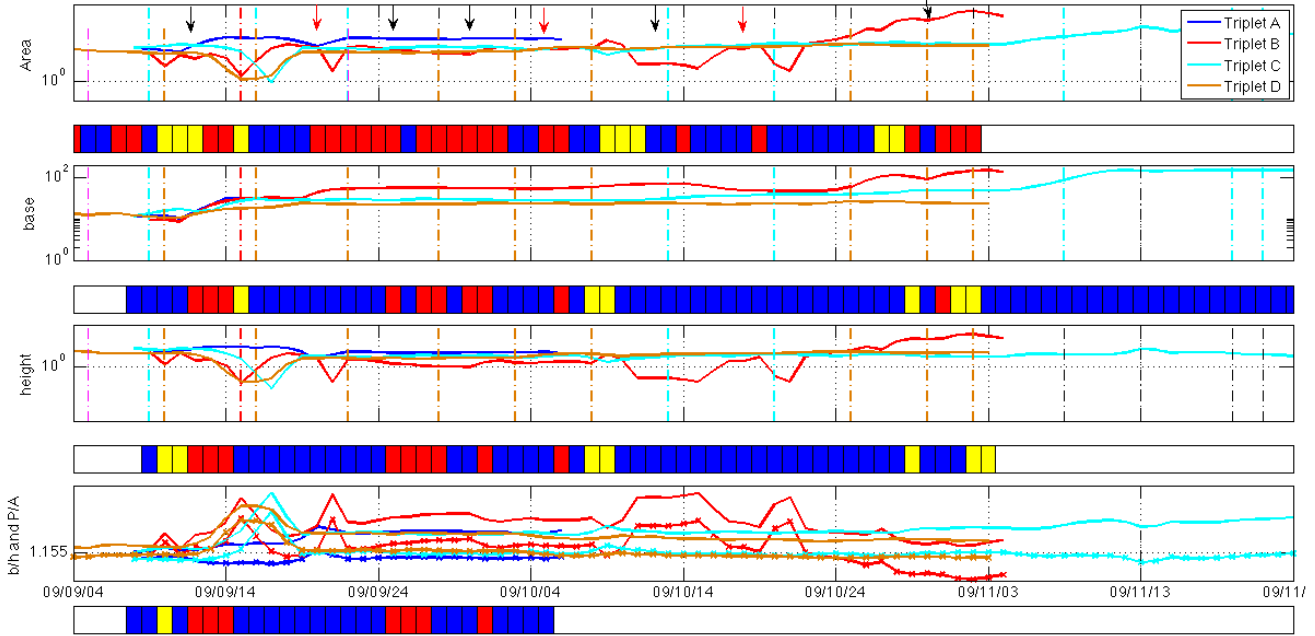
Figure 11: Triplet area evolution. Time series of triplet area, base, height, base-to-height and perimeter-to-area ratios for triplets A to D. Solid lines in lower panel depict the base-to-height ratio, while the lines with symbols depict the perimeter-to-area ratio. The value for the base-to-height ratio associated with an equilateral configuration (1.155) is also shown. Horizontal bar graphs depict on-, along-, and offshore ice drift as depicted in Figure 7.
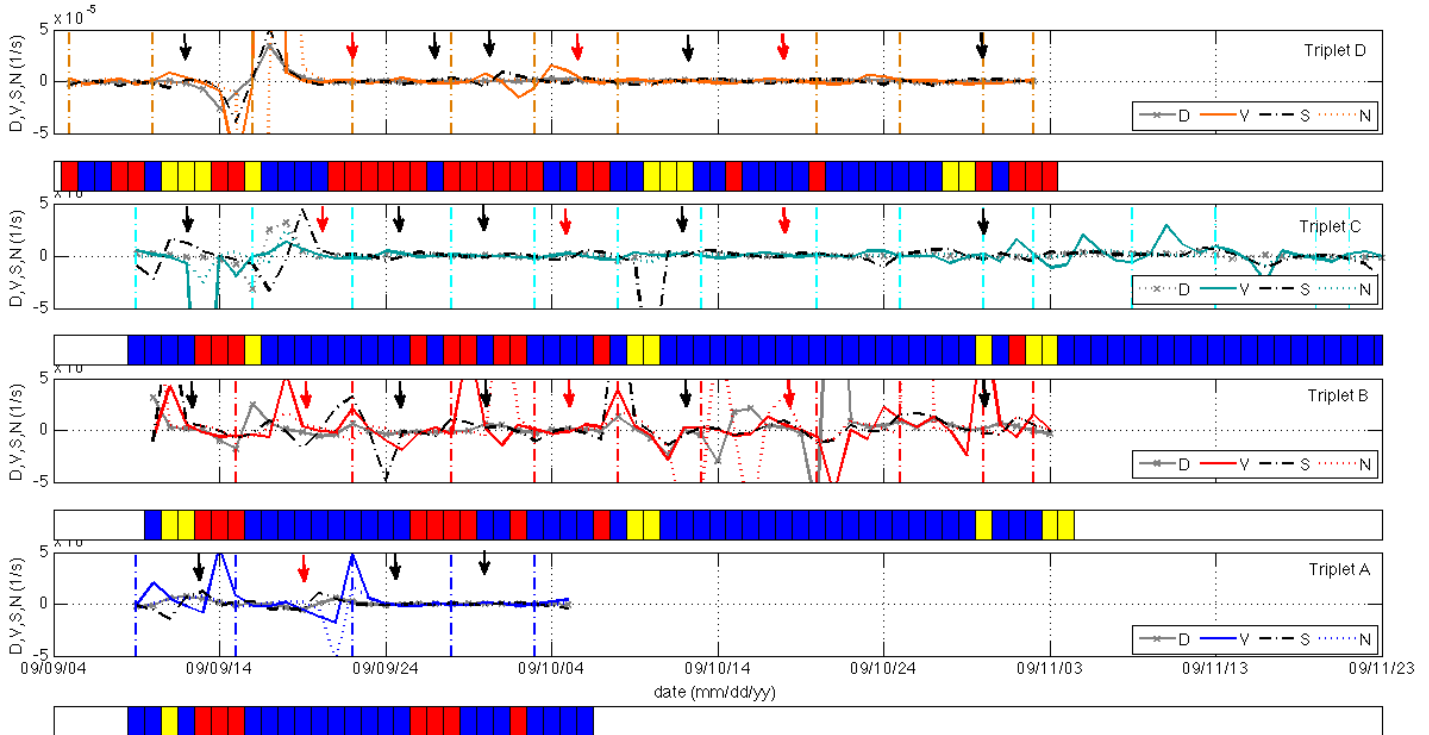
Figure 12: Sea ice deformation. Time series of Differential Kinematic Parameters (DKPs) divergence (D), vorticity (V), the shearing deformation rate (S), and the normal (stretching) deformation rate (N) for triplets A (lowermost panel) to D (uppermost panel). Vertical lines depict SLP high in the vicinity of each triplet centroid as shown in Figure 3. Horizontal bar graphs depict on-, along, and offshore ice drift as depicted in Figure 5.
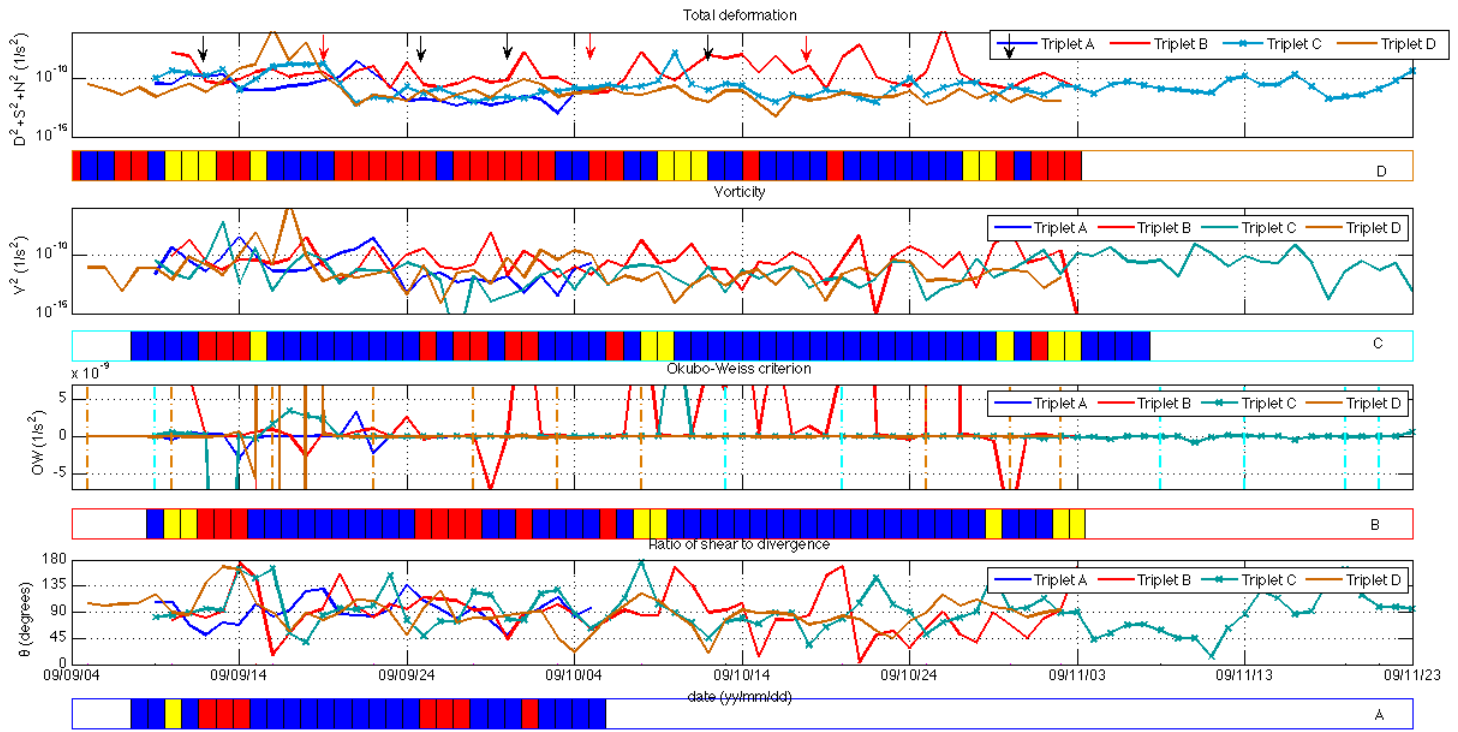
Figure 14: Relative sea ice deformation. Time series of relative sea ice deformation for Triplets A to D, including the total deformation ($D^2 + S^2 + N^2$), vorticity (V^2), Okubo-Weiss criterion capturing relative contributions of deformation and vorticity with OW > 0 indicating deformation-dominated flow and OW <0 indicating flow dominated by vorticity, and θ, or the arctan of the shear-to-divergence ratio to further distinguish deformation between shear and divergence-dominated regimes relevant for rheological characterizations.
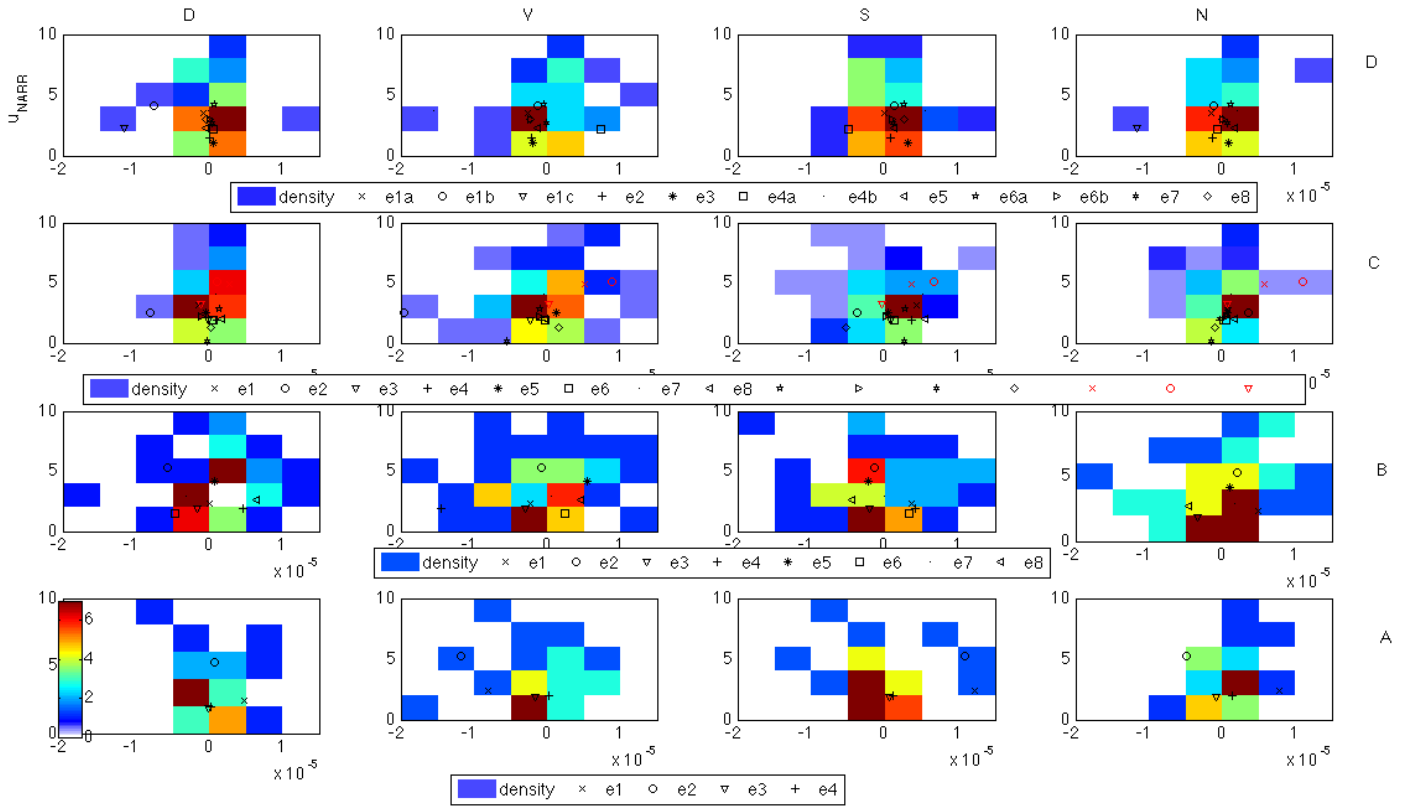
Figure 15: Scatter plots of NARR winds versus DKPs for triplets A to D showing number of triplet centroid values in the vicinity of and associated with NARR and DKP bins. Symbols depict directional change events.

Table 1: Evolution in triplet A to D trajectories; triplet event dates and coordinates

Event/Triplet	Date (mm/dd)		Latitude		Longitude	
e1 – Initial directional change event and cusp in trajectory						
A	09/11	09/13	72.68	72.71	-137.47	-137.64
B	09/11	09/13	72.76	72.65	-137.34	-137.47
C	09/11	09/13	73.14	73.18	-136.74	-137.14
D	09/13	09/15	73.18	73.04	-137.14	-137.32
	09/11	09/13	74.26	74.36	-135.89	-136.18
	09/13	09/15	74.36	74.22	-136.18	-136.25
e2 – Second event and southwestward migration						
A	09/18	09/20	72.57	72.46	-138.78	-139.72
B	09/18	09/20	72.65	72.62	-138.73	-139.74
C	09/19	09/21	72.96	72.88	-139.02	-139.75
D	09/21	09/23	74.02	73.95	-137.68	-137.84
e3 – Third event and southward migration						
A	09/24	09/26	72.43	72.33	-141.34	-141.61
B	09/24	09/26	72.48	72.45	-141.37	-141.64
C	09/24	09/26	72.82	72.72	-140.87	-141.07
D	09/26	09/28	72.72	72.65	-141.07	-140.86
	09/26	09/28	73.78	73.75	-137.80	-137.55

Event/Triplet	Date		Latitude		Longitude	
e4 – Fourth event and south- and westward migration						
A	09/29	10/01	72.22	72.14	-141.64	-142.15
B	09/29	10/01	72.39	72.32	-141.67	-142.17
C	09/29	10/01	72.62	72.52	-140.96	-141.44
D	09/28	09/30	73.75	73.62	-137.55	-137.89
	09/30	10/02	73.62	73.32	-137.89	-137.65
e5 – Fifth event and northwestward migration						
A	--	--	--	--	--	--
B	10/04	10/06	72.32	72.24	-143.09	-144.00
C	10/04	10/06	72.41	72.36	-142.24	-143.10
D	10/05	10/07	73.23	73.02	-138.46	-138.47
e6 – Sixth event and northwestward migration ; triplet D loop						
A	--	--	--	--	--	--
B	10/11	10/13	72.21	72.06	-146.08	-146.63
C	10/11	10/13	72.82	72.88	-144.83	-145.22
D	10/11	10/13	73.43	73.54	-139.63	-139.83
	10/13	10/15	73.54	73.47	-139.83	-139.57

Event/Triplet	Date		Latitude		Longitude	
e7 – Seventh event and northwestward migration						
A	--	--	--	--	--	--
B	10/17	10/19	72.07	71.98	-147.77	-148.65
C	10/17	10/19	72.97	73.04	-145.89	-146.62
D	10/17	10/19	73.46	73.42	-140.04	-140.55
e8 – Eighth event and northwestward migration; triplet C and D loop						
A	--	--	--	--	--	--
B	10/29	10/31	72.61	72.60	-156.67	-156.68
C	10/27	10/29	73.33	73.33	-152.50	-152.76
D	10/29	10/31	73.33	73.36	-152.76	-152.58
	10/27	10/29	73.61	73.71	-145.68	-145.92

Table 2: DKPs and impact on triangles

Triangle feature	DKPs			
	D	V	S	N
Area	D	x*	x	
Orientation	x	V		x
Shape	x	x	S	N

5   *x indicates that the DKPs do not change the triangle feature

Appendix A: Methodology to Derive Daily Positions, Triplet Arrays, Centroids, and Ice Drift from Telemetry Data

5   Geographical positions are recorded from global positioning (GPS) beacons explained in the data section. The observed temporal resolution of the beacon position data is two hours (dt = 2 hours). Daily average positions are calculated for the analysis and time series. The position data is subsequently used to compute drift components based on triplet centroid daily displacements.

A.1. Sea ice drift and triplet centroids

10   A four-step process was used to convert telemetry geographical position records into daily beacon averages, centroid locations, and sea ice drift. First, daily average positions were calculated from the two-hourly data for each beacon. Second, triplets were organized based on proximity to the coastline, inter-beacon distances, and overlapping time intervals. Triplets A and B, with two shared beacons, were selected to highlight differences in ice drift and deformation on scales comparable to inter-beacon

15   separations.

Third, centroids are calculated using the coordinates of the three beacons comprising each triplet. Fourth, ice drift is computed from centroid displacements. Specifically, the geographical latitude and longitude decimal degrees are converted to horizontal ortho-linear metric distances, using the north polar azimuthal equal-area map centred on the North Pole. Thus for the Earth's radius

$R = 6371.228\ km$, pixel size $C = 25.0675\ km$, latitude ϕ, longitude λ, row and column origin

$r0 = s0 = 181$ for a $361x361$ grid, and

$$r = 2R \sin \lambda \sin \left(\frac{\pi}{4} - \frac{\phi}{2} \right)$$
$$s = -2R \cos \lambda \sin \left(\frac{\pi}{4} - \frac{\phi}{2} \right),$$

the speeds associated with the metric distances, $u_r = 10^3 \Delta r / (\Delta t)$ and $u_s = 10^3 \Delta s / (\Delta t)$, for

$\Delta t = 24 \times 3600\text{(s)}$, are transformed to zonal and meridional components such that

$$u = u_r \cos \lambda + v_r \sin \lambda$$
$$v = -u_r \sin \lambda + v_r \cos \lambda.$$